© 2021. Published by The Company of Biologists Ltd | Development (2021) 148, dev199307. doi:10.1242/dev.199307

RESEARCH ARTICLE

Identification of disease-relevant modulators of the SHH pathway in the developing brain

Nora Mecklenburg[1,‡], Izabela Kowalczyk[1,‡], Franziska Witte[2,*,‡], Jessica Görne[1], Alena Laier[1], Tamrat M. Mamo[1], Hannes Gonschior[3], Martin Lehmann[3], Matthias Richter[4], Anje Sporbert[4], Bettina Purfürst[5], Norbert Hübner[2,6,7,8] and Annette Hammes[1,§]

ABSTRACT

Pathogenic gene variants in humans that affect the sonic hedgehog (SHH) pathway lead to severe brain malformations with variable penetrance due to unknown modifier genes. To identify such modifiers, we established novel congenic mouse models. LRP2-deficient C57BL/6N mice suffer from heart outflow tract defects and holoprosencephaly caused by impaired SHH activity. These defects are fully rescued on a FVB/N background, indicating a strong influence of modifier genes. Applying comparative transcriptomics, we identified *Pttg1* and *Ulk4* as candidate modifiers upregulated in the rescue strain. Functional analyses showed that ULK4 and PTTG1, both microtubule-associated proteins, are positive regulators of SHH signaling, rendering the pathway more resilient to disturbances. In addition, we characterized ULK4 and PTTG1 as previously unidentified components of primary cilia in the neuroepithelium. The identification of genes that powerfully modulate the penetrance of genetic disturbances affecting the brain and heart is likely relevant to understanding the variability in human congenital disorders.

KEY WORDS: SHH, Primary cilium, Forebrain development, Holoprosencephaly, Heart, Modifier genes

INTRODUCTION

Holoprosencephaly (HPE) is the most common structural defect of human forebrain development. HPE is characterized by impaired separation of the cerebral hemispheres and is typically accompanied by craniofacial malformations (Geng and Oliver, 2009; Hong and Krauss, 2018; Krauss, 2007; Ming and Muenke, 2002; Muenke and Beachy, 2000). During embryonic forebrain development, HPE can be induced by exposure to environmental toxins (Krauss and Hong, 2016; Weiss et al., 2018) or can be due to genetic predisposition with mono- or polygenic contributions (Krauss and Hong, 2016; Roessler and Muenke, 2010). Single mutations causing HPE have been identified (Hayhurst and McConnell, 2003; Roessler and Muenke, 2010; Roessler et al., 1996) and, among those, mutations in human sonic hedgehog (*SHH*) and its downstream effector genes account for at least 5% of autosomal dominant nonsyndromic HPE cases (Wallis and Muenke, 1999, 2000; Wallis et al., 1999). However, even within pedigrees carrying the same *SHH* mutation, HPE phenotypes vary among relatives and can range from alobar HPE, to facial abnormalities typical of HPE, to asymptomatic appearance of the carrier. Such intrafamilial variability of HPE phenotypes could be due to both environmental and genetic factors (Heussler et al., 2002; Hong and Krauss, 2018; Ming and Muenke, 2002; Muenke and Beachy, 2000; Muenke and Cohen, 2000; Roessler et al., 1996).

Studies on mouse models for HPE suggest that loss-of-function mutations in genes, relevant for forebrain development, result in brain and craniofacial anomalies that recapitulate HPE phenotypes in patients carrying mutations in the same genes (Geng and Oliver, 2009; Hayhurst and McConnell, 2003; Heyne et al., 2016; Hong and Krauss, 2018). Mice deficient for SHH develop forebrain defects resembling those of human HPE cases (Chiang et al., 1996). Intriguingly, the variability of HPE phenotypes found in humans is also reflected in gene-targeted mouse models, as phenotype penetrance often depends on the mouse strain (Anderson et al., 2002; Cole and Krauss, 2003; Geng and Oliver, 2009; Geng et al., 2008; Hong and Krauss, 2018; Petryk et al., 2004; Schachter and Krauss, 2008).

LRP2 (low-density lipoprotein receptor-related protein 2) is a component of the SHH signaling machinery in the primary cilium (Christ et al., 2012) and has been implicated in the etiology of HPE in mice and humans (Kim et al., 2019; Rosenfeld et al., 2010; Spoelgen et al., 2005; Willnow et al., 1996). Humans with autosomal recessive *LRP2* gene defects suffer from Donnai-Barrow syndrome, with clinical characteristics including heart anomalies (Pober et al., 2009), craniofacial anomalies, forebrain defects (Kantarci et al., 2007; Ozdemir et al., 2019) and microforms of HPE (Rosenfeld et al., 2010). In addition, severe forms of HPE in families presenting with oligogenic events involving *LRP2* have been identified (Kim et al., 2019), and inter- and intrafamilial phenotypic variability, which is a characteristic feature of HPE (Dubourg et al., 2018; Solomon et al., 2010), is observed in Donnai-Barrow syndrome (Khalifa et al., 2015; Longoni et al., 2008; Pober et al., 2009).

Here, we have analyzed two congenic mouse models of *Lrp2* that reflect the phenotypic variability of HPE in humans with *LRP2* mutations. Comparison of these *Lrp2*$^{-/-}$ strains allowed us to

[1]Disorders of the Nervous System, Max-Delbrück-Center for Molecular Medicine in the Helmholtz Association (MDC), 13125 Berlin, Germany. [2]Cardiovascular and Metabolic Sciences, Max Delbrück Center for Molecular Medicine in the Helmholtz Association (MDC), 13125 Berlin, Germany. [3]Cellular Imaging, Light Microscopy, Leibniz-Research Institute for Molecular Pharmacology (FMP), 13125 Berlin, Germany. [4]Advanced Light Microscopy Technology Platform, Max-Delbrück-Center for Molecular Medicine in the Helmholtz Association (MDC), 13125 Berlin, Germany. [5]Electron microscopy technology platform, Max-Delbrück-Center for Molecular Medicine in the Helmholtz Association (MDC), 13125 Berlin, Germany. [6]German Center for Cardiovascular Research (DZHK), Partner Site Berlin, 10785 Berlin, Germany. [7]Charité-Universitätsmedizin Berlin, 10117 Berlin, Germany. [8]Berlin Institute of Health (BIH), 10178 Berlin, Germany.
*Present address: Structural Biology, Lead Discovery, Nuvisan ICB, 13353 Berlin, Germany.
‡These authors contributed equally to this work

§Author for correspondence (hammes@mdc-berlin.de)

I.K., 0000-0002-1476-7531; A.H., 0000-0003-1663-8378

Handling Editor: James Briscoe
Received 11 December 2020; Accepted 19 July 2021

Development (2021) 148, dev199307. doi:10.1242/dev.199307

identify candidate modifier genes that affect SHH signaling in the primary cilium.

RESULTS

Genetic background determines penetrance of craniofacial, brain and heart defects in *Lrp2*$^{-/-}$ mutant mice

Lrp2$^{-/-}$ mice on a C57BL/6N background at embryonic stage (E) 18.5 displayed severe HPE-associated craniofacial dysgenesis (Fig. 1A). In particular, they showed cleft lip (Fig. 1A, arrow) and incompletely developed or even bilaterally or unilaterally absent eyes (Fig. 1A, asterisk). Further characteristic features in these mutants were a shortened skull and an open anterior suture (Fig. 1A, arrowhead). In contrast, *Lrp2*$^{-/-}$ congenic mice with a FVB/N background showed 100% penetrant rescue of all the above described craniofacial defects (Fig. 1A), except for a mild suture phenotype (Fig. 1A, arrowhead). HPE in *Lrp2*$^{-/-}$ C57BL/6N embryos, resulting from impaired ventral midline specification, was fully penetrant and characterized by a fusion of the cortical hemispheres (Fig. 1B, arrowheads) with a single lateral ventricle (Fig. 1B, arrow) and absent olfactory bulbs (Fig. 1B, asterisks). In contrast, HPE was fully rescued in all *Lrp2*$^{-/-}$ FVB/N mutants, which presented with correctly separated cortical hemispheres, olfactory bulbs and clearly defined lateral ventricles. Corpus callosum and the anterior commissure were present in the LRP2-deficient FVB/N mice (Fig. 1B).

LRP2-deficient C57BL/6N mice also suffer from cardiovascular anomalies, including a common arterial trunk (CAT) (Baardman et al., 2016; Christ et al., 2020; Li et al., 2015). Interestingly, there is comorbidity of HPE and congenital heart disease in individuals with variants of known HPE-related genes (Tekendo-Ngongang et al., 2020). *Lrp2*$^{-/-}$ embryos with a CAT display a single common coronary outflow artery vessel instead of a pulmonary artery and an ascending aorta. Less frequently, *Lrp2*$^{-/-}$ embryos displayed a double outlet right ventricle (DORV), in which the pulmonary artery and ascending aorta both connect to the right ventricle. We found that 15 out of 16 *Lrp2*$^{-/-}$ mutants on a C57BL/6N background displayed CAT (Fig. S1C,D,F′ and Table S1), and one remaining mutant embryo displayed a DORV (Table S1). The CAT phenotype was also visualized by colored liquid plastic injection (Fig. S1D, arrowhead), which indicated a CAT and a ventricular septum defect. We never observed a CAT in *Lrp2*$^{-/-}$ FVB/N mutants; 85% of *Lrp2*$^{-/-}$ FVB/N embryos showed no

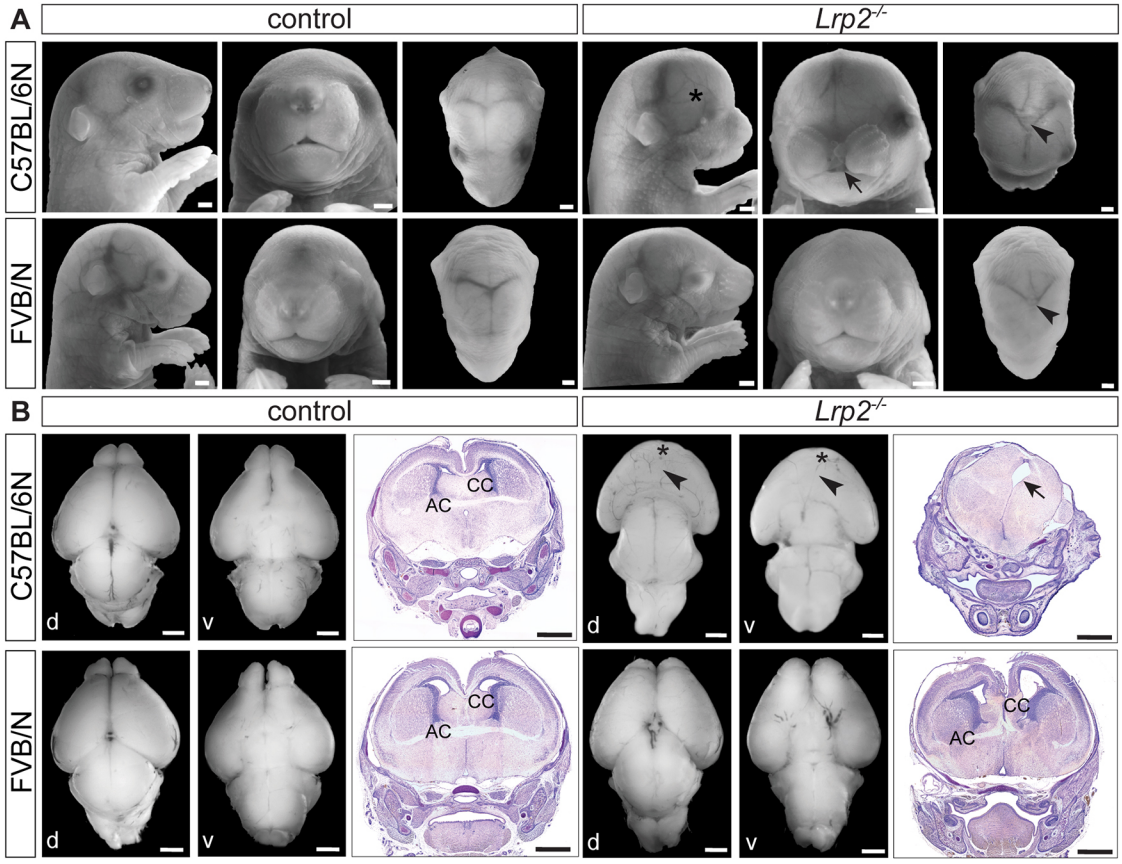

Fig. 1. Rescue of craniofacial malformations, HPE and heart defects in *Lrp2*$^{-/-}$ FVB/N mice. (A) *Lrp2*$^{-/-}$ C57BL/6N E18.5 embryos (*n*=30) with craniofacial defects: underdeveloped or missing eyes (asterisk), cleft lip (arrow) and hypertelorism. Dorsal view of the head revealed a shortened and widened skull with impaired suture formation and an open fontanelle (arrowhead). *Lrp2*$^{+/+}$ and *Lrp2*$^{+/-}$ littermates served as controls (*n*=66). *Lrp2*$^{-/-}$ FVB/N mutants (*n*=28) displayed normal skull formation, normal eyes and normal midface structures, comparable with controls (*n*=94). *Lrp2*$^{-/-}$ FVB/N embryos had a mild incomplete anterior fontanelle closure (arrowhead). Pigmentation of the retina is missing due to albinism in FVB/N. Scale bars: 1 mm. (B) Brains from E18.5 control and *Lrp2*$^{-/-}$ embryos in dorsal (d) and ventral (v) view, and Nissl-stained coronal sections. *Lrp2*$^{-/-}$ C57BL/6N brain with alobar HPE (arrowheads) (*Lrp2*$^{-/-}$ *n*=4; controls *n*=6). Olfactory bulbs were absent in mutants (asterisks). All sectioned *Lrp2*$^{-/-}$ C57BL/6N brains (*n*=13) showed alobar HPE with a single lateral ventricle (arrow) compared with controls (*n*=6). Corpus callosum (CC) and anterior commissure (AC) were missing in *Lrp2*$^{-/-}$ C57BL/6N mice. *Lrp2*$^{-/-}$ FVB/N embryos showed normal forebrain separation (*Lrp2*$^{-/-}$ *n*=5; controls *n*=3). Olfactory bulbs were present in *Lrp2*$^{-/-}$ FVB/N brains. All *Lrp2*$^{-/-}$ FVB/N sectioned brains (*n*=6) displayed normally separated ventricles, and a normal CC and AC comparable with controls (*n*=4). Scale bars: 1 mm.

Development (2021) 148, dev199307. doi:10.1242/dev.199307

apparent heart anomalies and a normal ventricular septum compared with controls (Fig. S1I,J,L,L′ and Table S1). Two out of 13 *Lrp2*$^{-/-}$ FVB/N mice showed a DORV (Table S1), which has been described in mutants on C57BL/6N strain at a similar frequency (Baardman et al., 2016). We conclude that the FVB/N background fully rescues the CAT phenotype, whereas the etiology of a DORV is not influenced by the strain background, suggesting the likelihood of divergent pathogenic mechanisms for a CAT and a DORV in *Lrp2*$^{-/-}$ mutants.

Rescue of SHH activity in neuroepithelial stem cells

In the neuroepithelium, LRP2 is located at the base of the primary cilium, where it teams up with patched 1 to mediate endocytic uptake and recycling of SHH (Christ et al., 2012). Consistent with our previous findings, *Lrp2*$^{-/-}$ C57BL/6N embryos showed normal SHH pattern in the prechordal plate, but little to no SHH in the overlying neuroepithelial stem cells compared with control embryos during the critical stages of forebrain specification at the 8-somite stage (Fig. 2B, 8 s). SHH protein was detected later in the neuroepithelium at the 11-somite stage, which is too late for proper ventral midline specification (Fig. 2B, 11 s). Intriguingly, all *Lrp2*$^{-/-}$ FVB/N mutants showed completely normal SHH localization throughout all developmental stages (Fig. 2B). To exclude a later onset of defects, we analyzed later embryonic stages. A fully penetrant hallmark of the *Lrp2*$^{-/-}$ C57BL/6N embryos at E10.5 is the lack of *Shh* RNA and protein in the telencephalon (Christ et al., 2012; Spoelgen et al., 2005) (Fig. 2C, arrowhead; Fig. S2A, arrowhead) and in the ventral midline of the diencephalon (Fig. S2B, arrowhead). *Lrp2*$^{-/-}$ FVB/N mutants showed normal *Shh* RNA expression and SHH protein localization in the ventral telencephalon and diencephalon (Fig. 2C, arrowhead; Fig. S2A,B).

Normal *Nkx2.1* expression pattern comparable with controls (Fig. S2G,H) confirmed proper activation of SHH downstream targets and intact ventral forebrain patterning in *Lrp2*$^{-/-}$ FVB/N mice (Fig. S2I,J), in contrast to mutants on a C57BL/6N background, which lacked *Nkx2.1* expression in the ventral forebrain (Fig. S2E,F) compared with controls (Fig. S2C,D). Thus, defects in the SHH pathway caused by loss of LRP2 were fully rescued on a FVB/N background. Consequently, the severe telencephalic vesicle separation defects in *Lrp2*$^{-/-}$ C57BL/6N mutants (Fig. S2K) did not manifest in mutants on a FVB/N background displaying properly separated forebrain hemispheres at E12.5 (Fig. S2K). Of note, *Lrp2*$^{-/-}$ mutants on both C57BL/6N and FVB/N backgrounds showed a more dilated and widened dorsal forebrain compared with the controls as shown in frontal views on whole embryos (Fig. S2K, asterisks) and on coronal sections (Fig. S2E,F,I,J, asterisks). The dilation of the dorsal neural tube is unrelated to impaired SHH function in the ventral neural tube and conserved between mouse strains and *Xenopus* with LRP2 loss of function (Kowalczyk et al., 2021).

Dominant effect of the FVB/N-specific transcriptome

To test a possible dominant effect of FVB/N-specific candidate modifier genes, we collected *Lrp2*$^{+/+}$ and *Lrp2*$^{-/-}$ first-generation hybrids from *Lrp2*$^{+/-}$ C57BL/6N×*Lrp2*$^{+/-}$ FVB/N parents (hereafter referred to as F1 embryos). Detailed phenotypic analyses of *Lrp2*$^{-/-}$ F1 embryos indeed revealed a full rescue of brain and craniofacial defects. They suffered from neither HPE nor

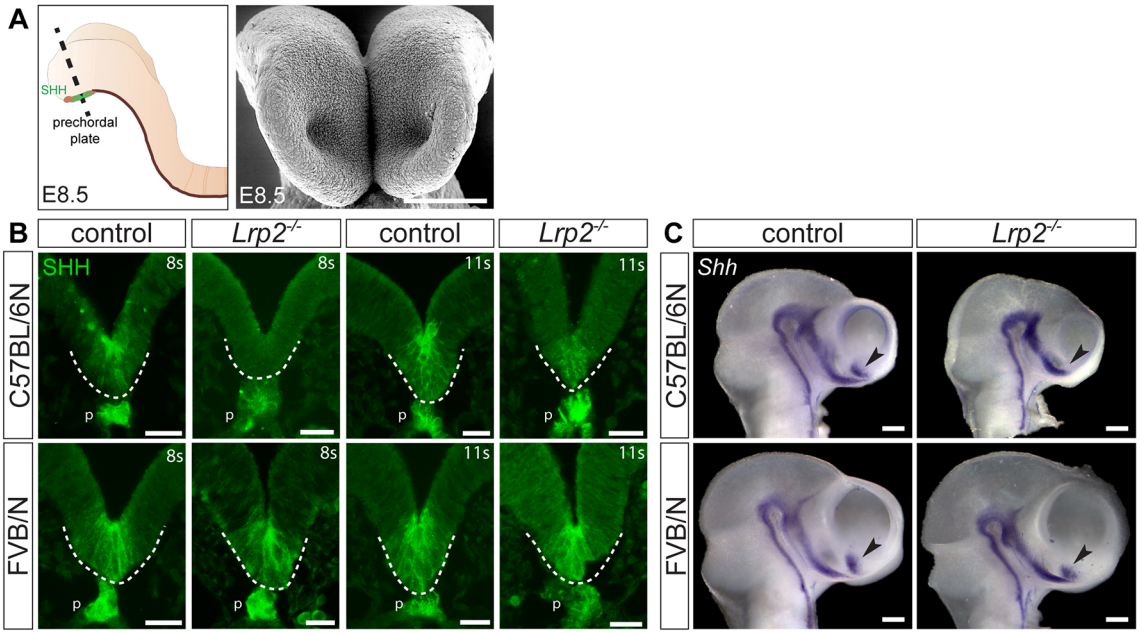

Fig. 2. Loss of SHH is rescued in the ventral forebrain of *Lrp2*$^{-/-}$ FVB/N embryos. (A) Schematic of E8.5 mouse embryo indicating the prechordal plate, underlying the neuroepithelium. Dotted line indicates section planes shown in B. Scanning electron microscopy image represents the front view of the developing neural folds. Scale bar: 100 µm. (B) Immunohistology for SHH on coronal sections of anterior neural folds in control (*Lrp2*$^{+/+}$ and *Lrp2*$^{+/-}$) and *Lrp2*$^{-/-}$ embryos on C57BL/6N and FVB/N backgrounds. In 8-somite stage (8 s) control embryos (n=7), SHH was detected in the prechordal plate (p) and in the neuroepithelium (above the dotted line). *Lrp2*$^{-/-}$ C57BL/6N embryos at 8 s (n=4) showed SHH in the prechordal plate, but little to no SHH in the neuroepithelium. In 11 s embryos, SHH appeared in the neuroepithelium of mutant embryos (n=3; n=4 for controls). *Lrp2*$^{-/-}$ FVB/N embryos (n=8 at 8-9 s, n=2 at 11 s) displayed a normal SHH expression pattern in the neuroepithelium throughout development, comparable with somite-matched control samples (n=10 at 8-9 s, n=8 at 11 s). Scale bars: 25 µm. p, prechordal plate; s, somites. (C) Whole-mount *in situ* hybridization for *Shh* on E10.5 embryonic heads. Controls (n=5) showed typical *Shh* expression pattern with a prominent signal in the telencephalon (arrowhead). *Lrp2*$^{-/-}$ C57BL/6N somite-matched embryos (n=9) had no telencephalic *Shh* signal (arrowhead). *Lrp2*$^{-/-}$ FVB/N embryos (n=8) displayed the same expression pattern as controls (n=4), including telencephalic *Shh* (arrowheads). Scale bars: 250 µm.

Development (2021) 148, dev199307. doi:10.1242/dev.199307

cleft lip (Fig. 3A and Fig. S3A). Analyzing the heart by stereomicroscopy, we never observed a common outflow tract in *Lrp2*$^{-/-}$ F1 embryos (0/27) at E18.5. Applying polymeric dye injection and histology revealed that 56% of the *Lrp2*$^{-/-}$ mutant F1 embryos had normal hearts and outflow tracts (Fig. S3E,F,G,G′ and Table S1). In 44% of the *Lrp2*$^{-/-}$ F1 embryos, we detected a DORV (Fig. S3H,I,J,J′ and Table S1).

As observed for the *Lrp2*$^{-/-}$ FVB/N embryos, all *Lrp2*$^{-/-}$ F1 embryos showed normal *Shh* expression in the developing forebrain, similar to control embryos (Fig. 3B, arrowheads). As HPE and SHH signaling defects were fully rescued in 100% of *Lrp2*$^{-/-}$ F1 embryos, we concluded that FVB/N allele-specific expression of yet unidentified genes has a dominant rescue effect. We hypothesize that such factors predispose neuroepithelial stem cells in FVB/N and F1 mice to maintain sufficient SHH signaling, despite the loss of LRP2, and thereby prevent HPE.

To identify factors conveying disease resistance, we next analyzed the transcriptome of *Lrp2*$^{+/+}$ and *Lrp2*$^{-/-}$ embryonic heads from C57BL/6N, FVB/N and F1 backgrounds (Fig. 3C). Performing DESeq2 differential expression analyses on all transcriptomes (Fig. 3D heatmap and Table S2), we detected 2170 differentially expressed genes (DEGs) between *Lrp2*$^{-/-}$ and *Lrp2*$^{+/+}$ embryos on a C57BL/6N background, only 367 DEGs for the FVB/N background and a similarly low number (241 DEGs) for the F1 background (Fig. 3E). Expression levels of HPE- and SHH pathway-related transcription factors such as *Vax1*, *Six6* and *Six3* were significantly decreased in *Lrp2*$^{-/-}$ C57BL/6N mutants compared with controls, but were unchanged in *Lrp2*$^{-/-}$ FVB/N mutants compared with FVB/N controls (Fig. 3F). In addition, the *Lrp2*$^{-/-}$ F1 mutants showed normal expression levels for *Vax1*, *Six6* and *Six3*, comparable with the *Lrp2*$^{+/+}$ controls (Fig. 3F), reflecting the rescue phenotype and suggesting a dominant effect of the FVB/N transcriptome.

Identification of strain-specific candidate modifier genes involved in ciliogenesis and SHH pathway regulation

To identify strain-specific candidate modifier genes and pathways underlying HPE susceptibility in C57BL/6N, and HPE rescue in FVB/N and F1, we used the transcriptome data set described above (Table S2). However, in this approach we focused on the strain-specific transcriptome differences. Thus, we compared gene expression between mutant *Lrp2*$^{-/-}$ samples on C57BL/6N, FVB/N and F1 backgrounds (Fig. 4A-E) and, most importantly, also between wild-type (*Lrp2*$^{+/+}$) samples comparing C57BL/6N,

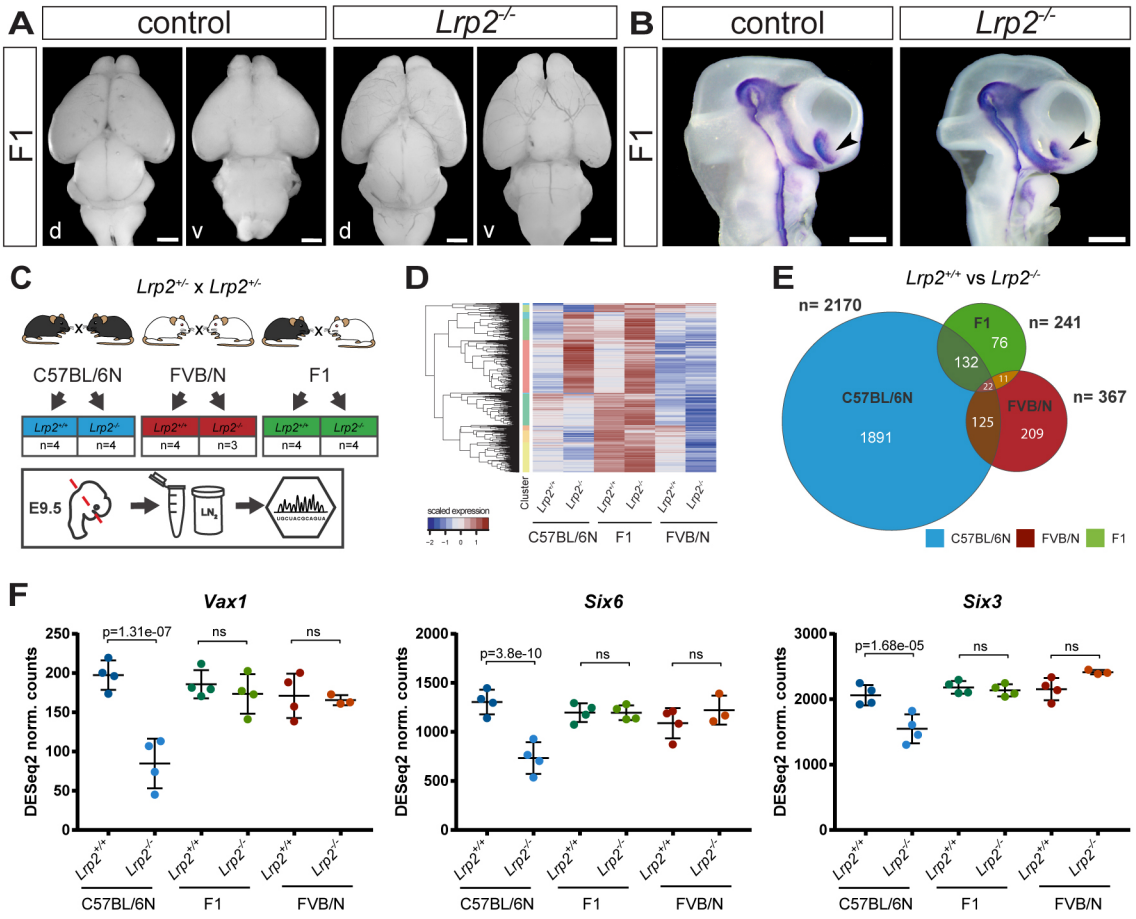

Fig. 3. Dominant effect of FVB/N-specific gene expression on phenotype penetrance. (A) Brains from E18.5 control (refers to *Lrp2*$^{+/+}$ and *Lrp2*$^{+/-}$; *n*=20) and *Lrp2*$^{-/-}$ F1 embryos (*n*=24) in dorsal (d) and ventral (v) view. *Lrp2*$^{-/-}$ F1 mice never displayed HPE (0/24) and showed normal separation of the forebrain hemispheres (24/24). Olfactory bulbs were present in *Lrp2*$^{-/-}$ F1 brains. Scale bars: 1 mm. (B) Whole-mount *in situ* hybridization for *Shh* on E10.5 embryonic heads. Controls (*Lrp2*$^{+/+}$ and *Lrp2*$^{+/-}$; *n*=6) and *Lrp2*$^{-/-}$ F1 embryos (*n*=8) showed a typical *Shh* pattern, including the telencephalic signal (arrowheads). Scale bars: 250 µm. (C) Collection of 24-somite stage *Lrp2*$^{+/+}$ and *Lrp2*$^{-/-}$ embryonic heads for RNA deep sequencing from C57BL/6N, FVB/N and F1 backgrounds. (D) Heatmap for RNA-sequencing results. (E) Venn diagram with numbers of DEGs comparing *Lrp2*$^{+/+}$ and *Lrp2*$^{-/-}$ samples on C57BL/6N, FVB/N and F1 backgrounds. The numbers of distinct and overlapping DEGs are shown. (F) DESeq2 normalized counts for *Vax1*, *Six6* and *Six3*. Data are mean±s.d.

Development (2021) 148, dev199307. doi:10.1242/dev.199307

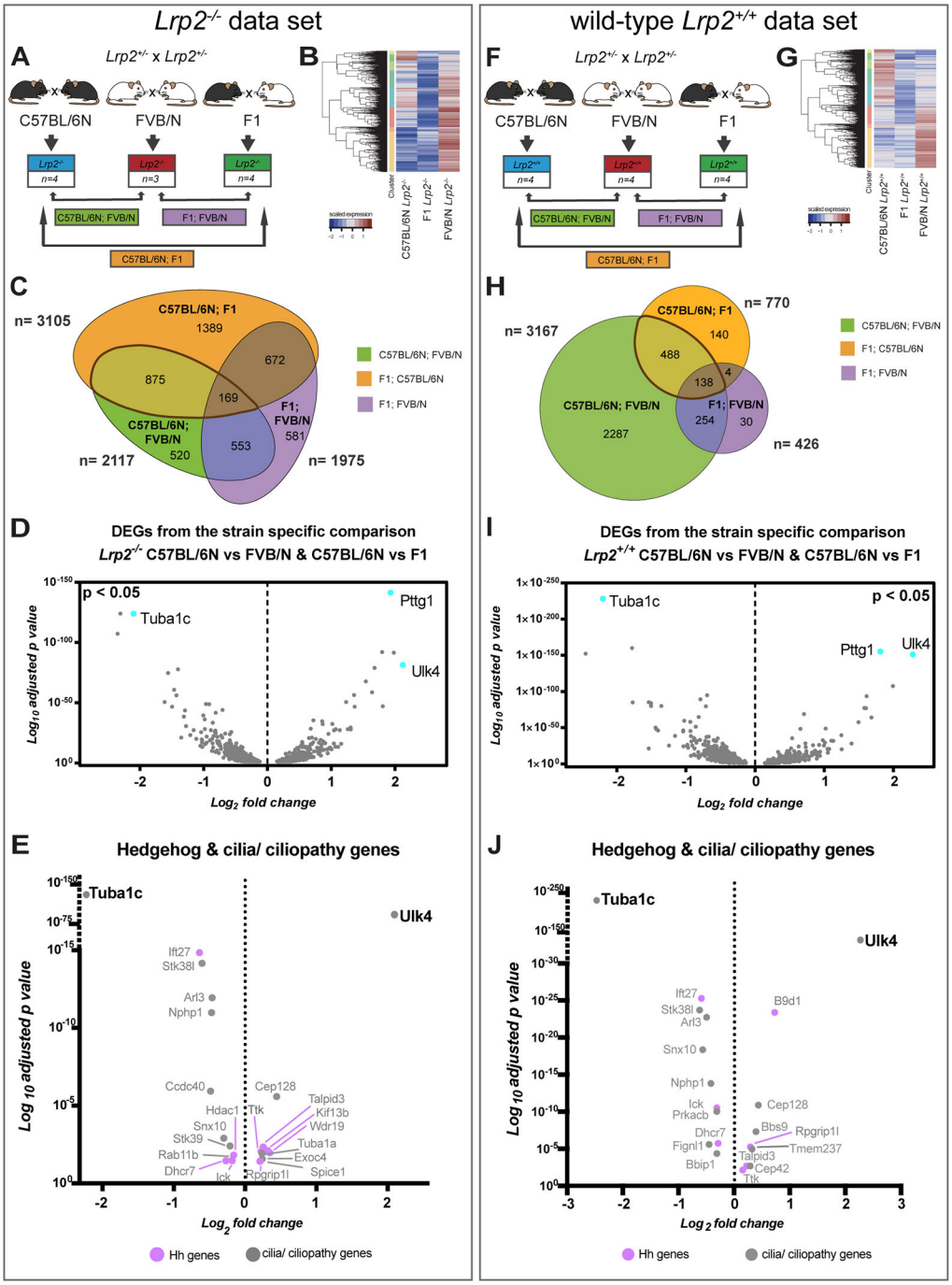

Fig. 4. Comparative transcriptome analysis identifies strain-specific expression of genes involved in ciliogenesis and SHH pathway regulation. (A,F) RNA deep sequencing analysis on *Lrp2*$^{-/-}$ (A) and wild-type *Lrp2*$^{+/+}$ (F) embryonic heads on C57BL/6N, FVB/N and F1 backgrounds. Comparison of the following expression profiles: C57BL/6N versus FVB/N, F1 versus FVB/N, and C57BL/6N versus F1. (B,G) Pattern of the *Lrp2*$^{-/-}$ (B) and *Lrp2*$^{+/+}$ (G) heat maps for all different strains. (C,H) Venn diagram (non-scaled) demonstrates the number of DEGs comparing *Lrp2*$^{-/-}$ samples (C) and wild-type *Lrp2*$^{+/+}$ samples (H). C57BL/6N versus FVB/N, F1 versus FVB/N, and C57BL/6N versus F1 comparisons are made [colored ellipses (C) and circles (H)]. Overlaps in two or three sets are indicated by the overlapping circles and by different color codes. (D,I) Volcano plots showing DEGs for *Lrp2*$^{-/-}$ samples (D) and *Lrp2*$^{+/+}$ samples (I) that were identified in both comparisons, C57BL/6N versus FVB/N as well as C57BL/6N versus F1 hybrids. (D) 562 genes were significantly downregulated and 482 genes were significantly upregulated in *Lrp2*$^{-/-}$ FVB/N and *Lrp2*$^{-/-}$ F1 embryonic heads compared with *Lrp2*$^{-/-}$ C57BL/6N samples. (I) 342 genes were significantly downregulated and 284 genes were significantly upregulated in *Lrp2*$^{+/+}$ FVB/N and F1 samples compared with C57BL/6N heads. (E,J) Cilia, ciliopathy and hedgehog signaling pathway-related genes after filtering DEGs from D and I, shown in volcano plots for *Lrp2*$^{-/-}$ (E) and *Lrp2*$^{+/+}$ (J) samples. Some of the cilia/ciliopathy genes are also hedgehog-related genes and therefore labeled in purple.

FVB/N and F1 backgrounds (Fig. 4F-J). Venn diagrams show the number of DEGs in *Lrp2*$^{-/-}$ embryos comparing the different backgrounds (Fig. 4C) and in wild-type *Lrp2*$^{+/+}$ embryos accordingly (Fig. 4H). Given the dominant effect of the FVB/N background, we focused on DEGs that were identified in both comparisons: C57BL/6N versus FVB/N and C57BL/6N versus F1 (Fig. 4D,I and Table S2). Importantly, out of the 1044 DEGs from the analysis comparing *Lrp2*$^{-/-}$ mutant samples, 426 DEGs were also identified in the wild-type *Lrp2*$^{+/+}$ comparisons (Table S2). Thus, these DEGs, which are common between mutant and wild-type comparisons of different strains, were not a consequence of LRP2 loss of function but were truly strain specific, and therefore met our criteria for strain-specific modifier candidates that can modulate signaling pathways in the wild-type situation.

As there was a clear effect on the SHH pathway in the ventral forebrain, we next filtered those DEGs with a known function in the SHH pathway, cilia or ciliopathies from our strain-specific datasets. Hedgehog and cilia/ciliopathy relevant genes were selected according to published data (Breslow et al., 2018; Pusapati et al., 2018), which include the Syscilia gold standard, and their expression was visualized by volcano plots (Fig. 4E,J and Table S3).

We determined that among cilia- and SHH-related genes, 12 were downregulated and 10 were upregulated in *Lrp2*$^{-/-}$ FVB/N and F1 samples compared with C57BL/6N (Fig. 4E). In the wild-type *Lrp2*$^{+/+}$ comparison, we identified 20 differentially expressed cilia- and SHH-relevant genes, of which 11 were upregulated and 9 were downregulated in wild-type FVB/N and F1 embryos compared with C57BL/6N (Fig. 4J).

Development (2021) 148, dev199307. doi:10.1242/dev.199307

For functional analyses we selected top hits, based on the highest fold change and *P*-value identified in both the mutant and wild-type comparisons (Fig. 4E,J). Tubulin α 1C (*Tuba1c*) and Unc-51-like kinase 4 (*Ulk4*) were highly differentially expressed in a strain-dependent manner.

Tuba1c, a component of tubulin, was expressed at five times lower levels in FVB/N $Lrp2^{-/-}$ and wild-type $Lrp2^{+/+}$ embryonic heads compared with both C57BL/6N genotypes (Fig. S4A). F1 samples also showed significantly lower expression levels than samples from the C57BL/6N strain (Fig. S4A). *Tuba1c* is listed in the database of ciliary genes (http://www.syscilia.org/goldstandard.shtml; Pusapati et al., 2018; van Dam et al., 2013) but data on its direct connection to the SHH pathway are limited. However, pathway analysis has linked *Tuba1c* to the SHH 'off' state (Fabregat et al., 2018; see also https://reactome.org/content/detail/R-HSA-5610787.1).

Ulk4, which belongs to a family of serine/threonine kinases, has been shown to regulate acetylation of α-tubulin, an important post-translational modification of microtubules (Lang et al., 2016). *Ulk4* was expressed at five and two times higher levels in FVB/N and F1 genotypes, respectively, compared with C57BL/6N samples (Fig. S4A).

ULK4 is a positive regulator of the SHH pathway localized to the primary cilium

We next analyzed the candidate modifier genes in a context independent of LRP2 loss of function. To test whether *Tuba1c* or *Ulk4* expression has functional effects on the SHH pathway, we used a dual luciferase reporter assay (Christ et al., 2012; Sasaki et al., 1997; Taipale et al., 2000; Zhang et al., 2006) and quantified activity of SHH signaling upon expression of modifier candidates. Expression of *B9d1*, a known SHH signaling modulator, was used as a positive control (Chih et al., 2012; Garcia-Gonzalo et al., 2011; Gerhardt et al., 2016). Overexpression of *B9d1* and *Ulk4*, respectively, in NIH-3T3 cells treated with SHH-Np resulted in a significant increase of SHH-responsive and GLI-driven relative luciferase levels compared with controls (Fig. 5A and Fig. S5A). The induction was inhibited by KAAD-cyclopamine, showing a specific effect on the canonical SHH pathway (Fig. 5A). In contrast, cells transfected with *Tuba1c* showed no increase in GLI-based luciferase activity after SHH stimulation compared with stimulated controls (Fig. 5A).

We validated the gain-of-function effect of ULK4 on the SHH pathway in human cells, using the hTERT RPE-1 cell line. *Ulk4* overexpression significantly increased endogenous GLI1 levels compared with controls after SHH stimulation (Fig. S5B-D).

To test the loss of function effect on the SHH signaling machinery, we performed knockdown experiments for ULK4 in NIH-3T3 cells and hTERT RPE-1 cells. Native *Gli1* mRNA and GLI1 protein levels were significantly lower in siRNA-treated cells, silencing *Ulk4* expression compared with control siRNA-treated cells after SHH stimulation (Fig. S5E-G). Furthermore, the induction of SHH-responsive and GLI-driven relative luciferase reporter activity was significantly compromised in ULK4 knockdown (KD) experiments compared with control siRNA treatment (Fig. 5B). To further evaluate the impact of ULK4 silencing in NIH-3T3 cells, we assessed SHH-induced ciliary Smoothened (SMO) localization comparing *Ulk4* siRNA and control siRNA-treated cells. SHH binding to PTCH1 allows SMO to accumulate in the ciliary membrane and to activate the pathway (Briscoe and Thérond, 2013). SHH-treated control cells showed a clear SMO enrichment in the cilium (Fig. 5C,D). In contrast, SHH-triggered ciliary SMO accumulation was significantly impaired in *Ulk4* siRNA treated cells (Fig. 5C-D′).

To address the issue of how ULK4 can modulate SHH signaling at the primary cilium, we next analyzed the subcellular localization of ULK4. The kinase was shown to be localized in the cytoplasm (Lang et al., 2014), which we also observed using confocal microscopy. However, co-immunostaining with acetylated tubulin also revealed localization of ULK4 to the primary cilium of NIH-3T3 cells (Fig. 5E). Furthermore, immunogold labeling for ULK4 on ultrathin sections of the mouse embryonic forebrain demonstrated localization of ULK4 to the basal body (Fig. 5F, arrowheads) and to the shaft of the primary cilium (Fig. 5F, boxed area). Based on the ULK4 gain- and loss-of-function experiments, as well as on the ciliary localization, we conclude that ULK4 is a positive regulator of the canonical SHH pathway that also leads to a significant reduction of pathway activation when silenced.

Identification of PTTG1 as a SHH pathway modifier

We next focused on highly regulated genes that had never hitherto been associated with the primary cilium and canonical SHH pathway, and went back to the unbiased set of DEGs. The transcript with the highest fold change value and most significant *P*-value was pituitary tumor transforming gene 1 (*Pttg1*), also known as securin (Fig. 4D,I). Higher *Pttg1* transcript levels (Fig. S4A) found in rescue backgrounds were reflected at the protein level. Western analysis detected significantly higher amounts of PTTG1 protein in FVB/N and F1 total embryos compared with C57BL/6N samples (Fig. S4B). In addition, we demonstrated significantly higher immunofluorescence intensities for PTTG1 in the FVB/N and F1 forebrain neuroepithelium compared with C57BL/6N (Fig. S4C).

We next tested whether PTTG1 can influence SHH signaling capacity. *Pttg1* overexpression in NIH-3T3 cells resulted in a significantly higher activation of the GLI luciferase reporter after SHH stimulation compared with control vector overexpression, and this was inhibited by KAAD-cyclopamine (Fig. 5A). Similar to *Ulk4*, *Pttg1* overexpression had a stronger effect on SHH pathway activation under conditions of lower stimulation, using 1:20 diluted SHH-conditioned medium (Fig. S5A). Additionally, *Pttg1* overexpression in hTERT RPE-1 cells significantly increased endogenous GLI1 levels after SHH stimulation (Fig. S5B), providing additional evidence for an enhancing effect of PTTG1 on SHH signaling strength.

We also performed knockdown experiments for PTTG1 in NIH-3T3 cells and hTERT RPE-1 cells. Silencing *Pttg1* expression had a significant negative effect on endogenous *Gli1* and GLI1 levels after SHH stimulation (Fig. S5E,G) and on SHH-responsive GLI-driven relative luciferase levels (Fig. 5B). Next, we assessed SHH-induced ciliary Smoothened (SMO) localization after silencing *Pttg1* expression. SMO concentration in the cilium was significantly lower in *Pttg1* siRNA-treated cells compared with controls after SHH stimulation (Fig. 5C-D′). Altogether, we observed clear and robust effects in PTTG1 gain-of-function experiments and a milder effect in our silencing experiments, where PTTG1 knockdown attenuated SHH pathway induction, but did not abolish SHH signaling.

We suggest that ULK4 and PTTG1, which are highly expressed in the FVB/N and F1 rescue backgrounds, are not necessary, but instead are enhancing components of the SHH machinery. This hypothesis is supported by our DESeq2 data and quantitative RT-PCR experiments, which showed a twofold increase in *Gli1* levels in the FVB/N rescue strain (Fig. 5G).

Development (2021) 148, dev199307. doi:10.1242/dev.199307

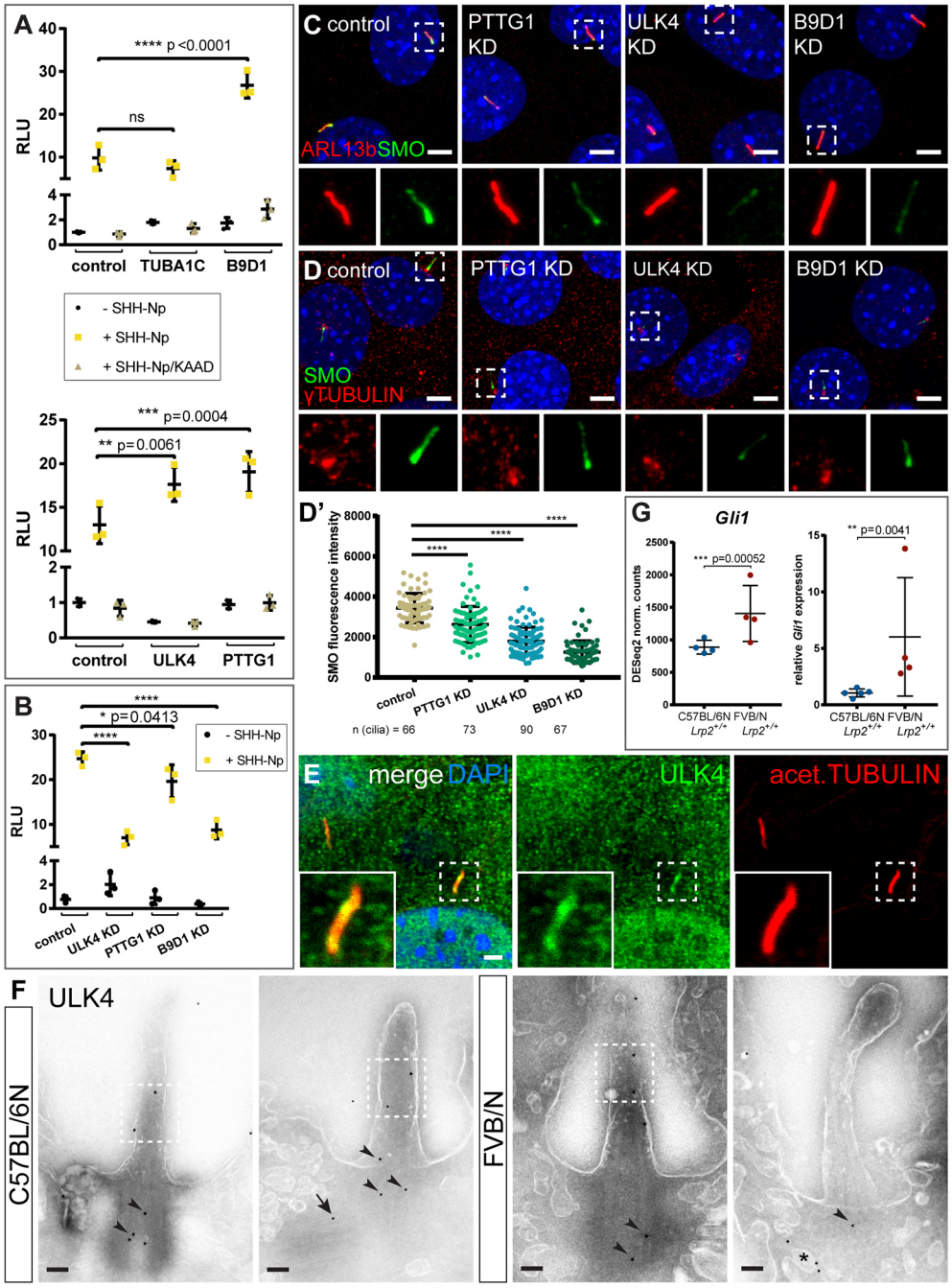

Fig. 5. ULK4 and PTTG1 are positive modulators of the SHH pathway. (A,B) SHH-responsive GLI-Luciferase reporter assay on NIH-3T3 cells. (A) Overexpression of *B9d1*, *Ulk4* and *Pttg1* resulted in a significant increase of relative luciferase levels compared with controls after SHH stimulation. *Tuba1c* overexpression showed no increase after SHH stimulation. NIH-3T3 cells were treated with medium containing SHH-Np or control medium. KAAD-cyclopamine was used to confirm the canonical SHH pathway response. Significance was assessed by two-way ANOVA; ***P*<0.01, ****P*<0.001; ns, not significant. RLU, relative light units. Data are mean±s.d. (B) ULK4, PTTG1 and B9D1 knockdown (KD) significantly compromised SHH-induced pathway activation compared with stimulated controls in the luciferase assay. Significance was assessed using two-way ANOVA: *****P*<0.0001. Data are mean±s.d. (C-D′) Knockdown experiments for ULK4, PTTG1 and B9D1 in NIH-3T3 cells. ARL13b (red, in C) and γ-tubulin (red, in D) immunostaining were used to visualize primary cilia and the base of the primary cilium, respectively. SHH induced ciliary Smoothened (SMO, green) immunocytochemistry in cells with control KD and candidate gene KD. DAPI (blue) marks nuclei. (C-D′) Representative micrographs (C,D) and corresponding quantification (D′) of endogenous SMO fluorescence intensity in the primary cilium. Data are mean±s.d. *****P*<0.0001 (one-way ANOVA). Boxed cilia are used for zoomed displays. Scale bars: 5 µm. (E) Confocal microscopy detected ULK4 immunostaining (green) in the cytoplasm of NIH-3T3 cells and in primary cilia (boxed), which are positive for acetylated tubulin (acet. tubulin, red). Scale bar: 2 µm. (F) Immunogold labeling of ULK4 in the forebrain neuroepithelium of wild-type C57BL/6N and FVB/N embryos at E9.5 showed clear localization of ULK4 at the microtubule-based axoneme in the shaft of the primary cilium (boxed), at the basal body of the cilium (arrowheads) and at the daughter centriole (arrow). ULK4 was also localized to the cytoplasm (asterisk). Scale bars: 100 nm. (G) DESeq2 normalized counts for *Gli1* showed significantly higher expression level for $Lrp2^{+/+}$ FVB/N compared with $Lrp2^{+/+}$ C57BL/6N samples. Relative mRNA expression level analysis by qRT-PCR confirmed significantly higher *Gli1* expression for $Lrp2^{+/+}$ FVB/N compared with $Lrp2^{+/+}$ C57BL/6N in E9.5 embryonic heads. $Lrp2^{+/+}$ C57BL/6N, *n*=5; $Lrp2^{+/+}$ FVB/N, *n*=4. Data are mean±s.d.

Development (2021) 148, dev199307. doi:10.1242/dev.199307

PTTG1 is a ciliary protein in the brain

We next analyzed the subcellular localization of PTTG1 and, as expected (Moreno-Mateos et al., 2011; Tong et al., 2008), we detected PTTG1 in the perinuclear region concentrated at the centrosome and in centrosomes of mitotic NIH-3T3 cells (Fig. 6A, arrow and arrowheads, respectively, and Fig. S6A, arrowheads). In some cells we also observed a dispersed PTTG1 signal in the cytoplasm (Fig. 6A, asterisk; Fig. S6A, asterisks). Interestingly, in non-mitotic NIH-3T3 cells, we detected PTTG1 in the primary cilium, a microtubule-based organelle, essential for SHH signaling. PTTG1 localized to a subset of primary cilia (Fig. 6B, arrowheads and Fig. S6B). We found PTTG1 in the periciliary region (Fig. 6C) as well as along the shaft of the primary cilium (Fig. 6D,E). Within the shaft PTTG1 protein localization was heterogenous, sometimes covering only the base or proximal region of the cilium (Fig. 6D and Fig. S6B,C) and in other cases the entire ciliary shaft (Fig. 6E). The variable localization of PTTG1 among different cilia suggested that it is not a structurally required component of the primary cilium, but might be shuttled into the shaft in a regulated fashion to support ciliary function. Ciliary localization for PTTG1 was confirmed in human hTERT RPE-1 cells (Fig. 6F), where PTTG1 was clearly localized to the shaft of the primary cilium. We further analyzed whether PTTG1 is also localized to cilia of the developing brain using cephalic explants from wild-type embryos (Fig. S7A). In neuroepithelial stem cells from both mouse strains, we detected PTTG1 localization to a subset of primary cilia (Fig. 7A, arrowheads; Fig. S7B) in the periciliary region (Fig. 7B,E) and in the shaft of the primary cilium labeled for ARL13b (Fig. 7C,D,F,G).

Ultrastructural analysis revealed that PTTG1 was localized to the microtubule-based ciliary axoneme (Fig. 7H and Fig. S7C, boxed), to the periciliary region at the appendages (Fig. 7H, arrowhead and Fig. S7C, arrowheads) and to the basal body (Fig. 7H, arrow and Fig. S7C, arrow). PTTG1 localization at the base of and in the primary cilium is depicted in a graphical model (Fig. 7J). Taken together, our results identified PTTG1 as a microtubule-associated component of the primary cilium that can modulate efficiency of the canonical SHH signaling pathway.

Cilia number and length differ between neuroepithelial stem cells from C57BL/6N and FVB/N wild-type strains

Analyzing neuroepithelial stem cells from C57BL/6N and FVB/N cephalic explants revealed differences in cilia number per area (Fig. S7B) and in cilia length between the strains (Fig. 7I). Calculating the number of cilia in the anterior neural tube on the apical surface of the explants, we identified 645 cilia/mm^2 surface area in FVB/N compared with 425 cilia/mm^2 surface area in C57BL/6N explants (Fig. S7B). We also used super-resolution gated STED microscopy to image anterior neural tube explants from E9.5 C57BL/6N and FVB/N mice labeled for the regulatory GTPase ARL13b, which is localized to the membrane of the entire ciliary shaft (Fig. 7I). Strikingly, wild-type neuroepithelial stem cells of the rescue strain FVB/N had 20% shorter primary cilia, with an average length of 1.19±0.01 µm (s.e.m.) compared with the primary cilia of the HPE-susceptible strain C57BL/6N, with an average length of 1.49±0.014 µm (Fig. 7I).

DISCUSSION

Lrp2$^{-/-}$ mutant mice studied on a C57BL/6N, a mixed C57BL/6N; 129/SvEMS-Ter, a CD1 and a C3H/HeNcrl background show fully penetrant forebrain defects and perinatal lethality (Sabatino et al., 2017; Spoelgen et al., 2005; Willnow et al., 1996). We and others previously found that a *Lrp2*$^{267/267}$ ENU mutant line on a

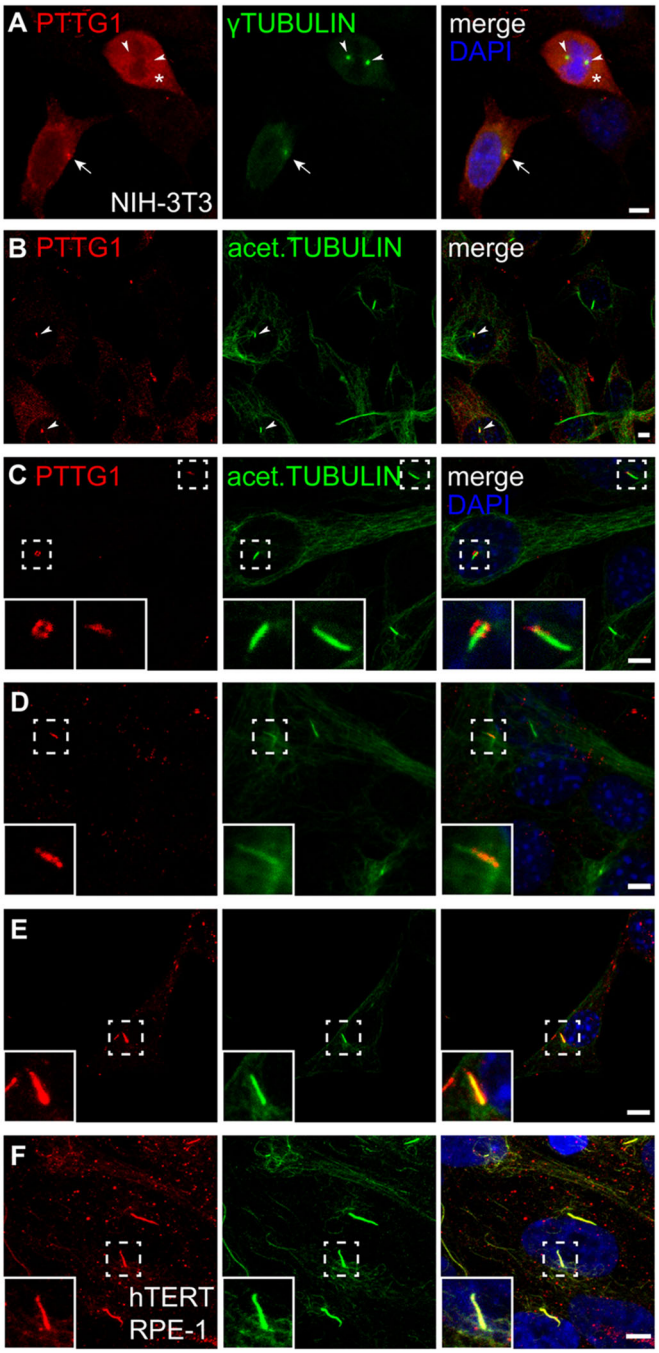

Fig. 6. PTTG1 is a ciliary component. (A-F) Subcellular localization of PTTG1 (red) and γ- or acetylated tubulin (green) in NIH-3T3 (A-E) and hTERT RPE-1 (F) cells, respectively, by immunocytochemistry using a knockout-validated antibody. (A) Confocal microscopy detected PTTG1 in mitotic cells at the perinuclear region, concentrated at the centrosome and centrosomes (arrow and arrowheads), which are positive for γ-tubulin (green), and in the cytoplasm (asterisks). (B) Interphase/quiescent cells showed PTTG1 localized to a subset of primary cilia (arrowheads), stained with acetylated tubulin (acet. tubulin, green). (C-E) PTTG1 localized to a subset of primary cilia, visualized by acetylated tubulin immunostaining, in a heterogeneous pattern. PTTG1 was detected in the periciliary region (C) and along the ciliary shaft, either at the proximal part (D) or covering entire cilium (E). (F) Ciliary localization of PTTG1 in hTERT RPE-1 cells. Image shows several cilia, visualized by acetylated tubulin (green), positive for PTTG1 (red). Insets show the magnification of the outlined cilium. All experiments were repeated at least five times in triplicate. DAPI (blue) marks nuclei. Scale bars: 5 µm.

Development (2021) 148, dev199307. doi:10.1242/dev.199307

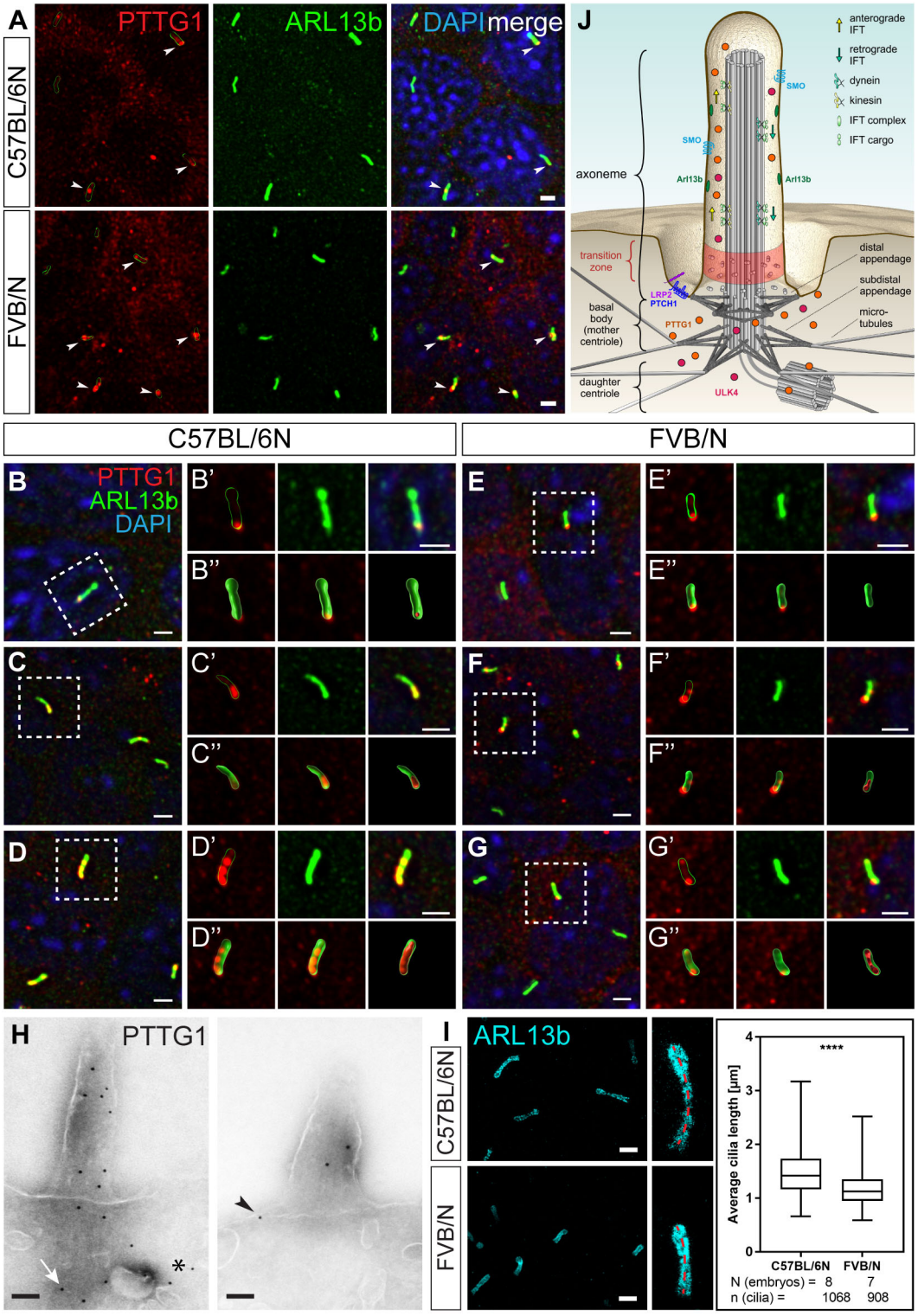

Fig. 7. See next page for legend.

predominant FVB/N background survived to adulthood (Gajera et al., 2010; Zarbalis et al., 2004; Zywitza et al., 2018). These studies prompted us to perform more-rigorous studies using a pure congenic *Lrp2*$^{-/-}$ FVB/N line to analyze the molecular mechanisms underlying these rescue effects.

Here, we demonstrate that the FVB/N background rescued HPE, which results from defects in the induction of the ventral forebrain, and most importantly rescued the underlying SHH signaling defects. Additionally, the previously described heart outflow tract phenotype of *Lrp2*$^{-/-}$ C57BL/6N mice (Baardman et al., 2016; Li et al., 2015) did not manifest in *Lrp2*$^{-/-}$ FVB/N embryos. Thus, genetic background strongly modifies the severity of congenital forebrain and heart defects in LRP2-deficient mice. The mouse models, described in this study, reflect the highly variable clinical

Development (2021) 148, dev199307. doi:10.1242/dev.199307

Fig. 7. PTTG1 is a ciliary component in neuroepithelial stem cells. (A) Confocal microscopy on the E9.5 C57BL/6N (n=6) and FVB/N (n=6) cephalic explants shows PTTG1 (red) in a subset of ARL13b-positive (green) primary cilia (arrowheads). Scale bars: 1 µm. (B-G) High-resolution confocal 3D imaging: PTTG1 is present in the periciliary region (B,E) and in the ciliary shaft (C,D,F,G). Top panel insets (B′-G′) show magnified cilia (outlined in B-G) with single signals for PTTG1 (left, outlining the cilium), ARL13b (middle) and merge (right). Bottom panel insets (B″-G″) show the same cilia as follows: reconstruction of ARL13b with non-reconstructed PTTG1 signal (left), optical section through this (middle) and reconstruction of both ARL13b and PTTG1 (right). Scale bars: 1 µm. (H) Immunogold labeling of PTTG1 in the forebrain neuroepithelium of E9.5 embryos showed clear localization of PTTG1 at the microtubule-based axoneme in the shaft of the primary cilium. PTTG1 was also localized to the daughter centriole (arrow). PTTG1 was also detected in the periciliary region (arrowhead) and a few signals were detected in the cytoplasm (asterisk). Scale bars: 100 nm. (I) Differences in primary cilia length comparing C57BL/6N and FVB/N neuroepithelial stem cells. Primary cilia, immunolabeled for ARL13b (blue), were imaged in the anterior region of E9.5 cephalic explants using STED microscopy. Primary cilia of $Lrp2^{+/+}$ FVB/N embryos (n=7) were 20% shorter [1.19±0.011 µm (s.e.m.); n=908] compared with cilia from $Lrp2^{+/+}$ C57BL/6N (n=8) samples [1.49±0.014 µm (s.e.m.); n=1068]. Cilia length was measured as indicated by red dashed lines. The box plot represents mean cilia length with whiskers indicating minimal and maximal values; unpaired t-test for statistical analysis; ****P<0.0001. Scale bars: 1 µm. (J) Schematic of the primary cilium with components relevant to the present work. PTTG1 and ULK4 are ciliary components, localized to the periciliary region and the ciliary shaft.

manifestation of HPE that is observed even among family members carrying the same pathogenic gene variant (Heussler et al., 2002; Hong and Krauss, 2018; Krauss, 2007; Muenke and Beachy, 2000; Roessler et al., 2018).

Identification of modifier genes in humans is challenging. It is also difficult to distinguish between the impact of modifier genes and environmental factors on the clinical variability. Comparing LRP2-deficient embryos on a susceptible C57BL/6N and a resistant FVB/N mouse strain allowed us to identify disease-relevant candidate modifiers. Background modifier studies in early embryonic development, where the FVB/N strain was analyzed, are rare and could yet shed important light on the etiology of neural tube defects as reviewed by Leduc et al. (2017). Exencephaly in *Cecr2* mutant mice shows strain-specific differences in penetrance, comparing BALB/cCrl and FVB/N, with the latter being a rescue background. Whole-genome linkage analysis revealed chromosome 19 as a modifier locus (Banting et al., 2005; Davidson et al., 2007; Kooistra et al., 2011).

In our study, we combined complex transcriptome and functional analyses to identify disease-relevant candidate modifiers. As we had documented a full rescue of HPE in FVB/N and F1, suggesting a dominant effect of FVB/N alleles, candidate modifier genes should be found in the overlapping pool of strain-specific DEGs, comparing C57BL/6N versus FVB/N and C57BL/6N versus F1 (Fig. 4C,H).

We identified *Tuba1c* and *Ulk4* as the top down- and upregulated DEGs, respectively, among the unfiltered DEGs (Fig. 4D,I) and among the hedgehog pathway/cilia gene-filtered DEGs (Fig. 4E,J). Functional data on *Tuba1c* regarding ciliogenesis or SHH pathway regulation are very limited. In the Reactome Pathway Knowledgebase, *Tuba1c* is linked to the hedgehog (HH) 'off', state suggesting that this tubulin plays a role as a negative regulator in the SHH pathway (Fabregat et al., 2018; see also https://reactome.org/content/detail/R-HSA-5610787.1).

Ulk4 is postulated to play an essential role in brain development and has been genetically linked to increased susceptibility in humans to developing schizophrenia (Lang et al., 2014). Mice with *Ulk4* gene defects show hydrocephaly, dilated brain ventricles and ependymal motile ciliary defects (Liu et al., 2016). Motile cilia defects in ULK4-deficient mice are characterized by defects in basal body orientation and axonemal organization, suggesting an important role for ULK4 in ciliary function (Liu et al., 2016). However, ULK4 function has not been associated with the SHH pathway or the primary cilium before.

Here, we demonstrate a previously unknown function for ULK4 as it can enhance canonical SHH signaling capacity in a heterologous system (Fig. 5A and Fig. S5A,B) and is present in the primary cilium with a prominent signal in the basal body (Fig. 5F). Downregulation of ULK4 attenuated SHH-induced pathway activation and impaired ciliary SMO accumulation (Fig. 5B-D and Fig. S5E-G). The exact mechanism of how ULK4 modifies SHH pathway activity at the primary cilium still needs to be identified. It is hypothesized that ULK4 regulates neuronal function by acetylation of α-tubulin, an important post-translational modification of microtubules (Lang et al., 2014, 2016). It is therefore feasible to hypothesize that ULK4 is required for efficient microtubule nucleation at the basal body during ciliogenesis. Altogether, our data suggest that ULK4 might regulate the penetrance of SHH-related congenital disorders.

In an unbiased approach, we asked whether the other top regulated DEG, *Pttg1* (Fig. 4D,I), could potentially also affect SHH activity. PTTG1 is a known substrate for the anaphase-promoting complex (APC) and associates with separin until activation of the APC (Hagting et al., 2002; Mei et al., 2001; Thornton and Toczyski, 2003; Yanagida, 2000). Various functions for PTTG1 have been described, including control of mitosis, DNA repair, transcriptional activity and cell migration (Genkai et al., 2006; Havens and Walter, 2011; Hellmuth et al., 2020; Holt et al., 2008; Xiang et al., 2017; Yan et al., 2015; Zheng et al., 2015). The protein has tumorigenic activity and the gene is amplified in various human tumors of the breast, uterus, lung and thyroid (Bernal et al., 2002; Mirandola et al., 2015; Read et al., 2017; Vlotides et al., 2007; Zou et al., 1999). High expression of *Pttg1* has also been associated with aggressive forms of brain tumors, including medulloblastoma and glioblastoma (Salehi et al., 2013; Yan et al., 2015). During embryonic development *Pttg1* expression has been reported in the human and murine brain (Boelaert et al., 2003; Karsten et al., 2003; Tarabykin et al., 2000). A recent study demonstrated a role of PTTG1 in microtubule nucleation (Moreno-Mateos et al., 2011). However, PTTG1 has hitherto not been associated with microtubule-based axoneme function of the primary cilium or with canonical SHH pathway modulation in the cilium. We show that *Pttg1* overexpression can indeed modulate SHH responsiveness (Fig. 5A and Fig. S5A,B). Therefore, we conclude that PTTG1 is a SHH pathway component and can promote canonical SHH signaling efficiency. We also discovered a previously unidentified and seemingly dynamic localization of PTTG1 to the periciliary region and to the microtubule-based axoneme of the cilium in NIH-3T3 and in neuroepithelial cells of the developing brain. The ciliary localization supports the hypothesis that PTTG1 modulates the SHH pathway via a cilia-associated mechanism. So far, only a relatively small number of regulatory proteins have been reported to be involved in both cytokinesis and ciliogenesis (Gromley et al., 2005; Kim et al., 2005; Pan et al., 2007; Park et al., 2008; Shah et al., 2008; Smith et al., 2011; Spektor et al., 2007; Vertii et al., 2015; Zuo et al., 2009). The anaphase-promoting complex (APC), which is important for cytokinesis, is found to be also localized to the basal body of the primary cilium during interphase, where its activity regulates disassembly of the primary cilium (Wang et al., 2014).

Development (2021) 148, dev199307. doi:10.1242/dev.199307

Our data provide evidence that PTTG1, besides its function as a cell cycle regulator associated with the centrosome, also plays a role in ciliogenesis and ciliary function. We propose that higher expression levels of PTTG1 predispose neuroepithelial stem cells in FVB/N mice to more efficient SHH signaling by enhancing microtubule repolymerization of the ciliary axoneme after cell division (Moreno-Mateos et al., 2011). Knockdown of PTTG1 has been shown to attenuate microtubule repolymerization after nocodazole treatment, which leads to microtubule depolymerization (Moreno-Mateos et al., 2011). Efficient microtubule repolymerization after cell division is crucial for assembly of the primary cilium and therefore SHH signaling (He et al., 2017). In our study, enhanced ciliogenesis is also supported by the on average higher number of cilia per area in the FVB/N neuroepithelium compared with C57BL/6N (Fig. S7B).

Interestingly, all three top regulated candidate modifier genes, *Tuba1c*, *Ulk4* and *Pttg1*, identified in our screen, are linked to microtubule nucleation and function, suggesting that the expression profile of these genes in a FVB/N background provides an advantageous environment for the microtubule-based ciliary function and SHH signaling, and ultimately a protective effect against developmental defects.

ULK4 and PTTG1 are not necessary for establishing SHH signaling as our silencing experiments attenuated, but did not abolish, SHH signaling. Additionally, *Ulk4*- and *Pttg1*-null mutant mice do not display phenotypes related to a complete loss of SHH activity (Liu et al., 2016; Wang et al., 2001). However, ULK4 and PTTG1 have positive effects on the overall efficiency of the pathway and can enhance SHH signaling strength, as shown in this article. Expression profiles of these candidate modifier genes and of other still functionally uncharacterized modifier candidates most likely ensure sufficient SHH activity in the absence of LRP2 on a FVB/N background.

Differences in ciliary factors between the strains could also be reflected in different morphology of primary cilia. Indeed, our super-resolution imaging revealed striking differences in the morphology of primary cilia between C57BL/6N and FVB/N neuroepithelial stem cells (Fig. 7I), suggesting that the genome of wild-type mice from different mouse strains has a substantial influence on the shape of primary cilia. This could have functional consequences and relevant clinical implications, considering the complex signaling function of the primary cilium (Gigante and Caspary, 2020; Goetz and Anderson, 2010; Nachury and Mick, 2019; Singla and Reiter, 2006). Little is known about the regulation of cilia length and the implication of variable cilia length in health and disease, including ciliopathies (Fliegauf et al., 2007; Gerdes et al., 2009). Interactions of ciliary components, e.g. prominin with ARL13b, have been shown to play a role in maintenance of length of the primary cilia throughout the animal kingdom (Jászai et al., 2020). Studies in mammalian cells suggest that increased soluble tubulin production leads to longer cilia and cytosolic tubulin stabilization results in shorter cilia (Sharma et al., 2011; Wang and Dynlacht, 2018; Wang et al., 2013). Wang et al. showed that the complex formed by cell cycle regulator APC and its co-activator Cdc20 at the basal body maintains optimal ciliary length and is crucial to shorten the cilia when cells exit from quiescent stage (Wang et al., 2014). As PTTG1 is a substrate for APC (Mei et al., 2001; Yanagida, 2000), and also found at the base of the cilium in our study, this conceptually links the function of PTTG1 to cilia length regulation.

We conclude that the FVB/N inbred mouse strain has advantageous ciliary composition and morphology, and we identify plausible molecular candidates that render the strain more resilient to disturbances of the SHH pathway during early development (Fig. 8). Our study highlights the importance of mouse strain-dependent penetrance of phenotypes and the role of modifier genes. As much as the FVB/N strain appears to be more resilient to forebrain patterning defects, as shown in this study, and to neural tube closure defects (Leduc et al., 2017), it is also commonly known that the FVB strain is more susceptible to mammary tumors whereas the C57BL/6 strain is more resistant (Davie et al., 2007). It will be interesting to test whether *Pttg1* and *Ulk4*, as SHH pathway stimulators, could be modifier genes that also modulate the mammary tumorigenesis in mouse models of breast cancer.

The expression profiles that differ profoundly between various wild-type strains during early developmental stages provide a unique resource that, to our knowledge, has not been available before. Considering the huge effects of the FVB/N background, this resource is particularly valuable to understand genetic robustness in brain and heart development. Furthermore, we show that genetics in the mouse combined with functional cell biological studies can define novel molecular mechanisms that potentially underlie variability in the penetrance of human cilia-associated neurodevelopmental disorders. Identification of disease relevant modifier genes in the mouse can provide important insights into the etiology and prevention of human congenital disorders.

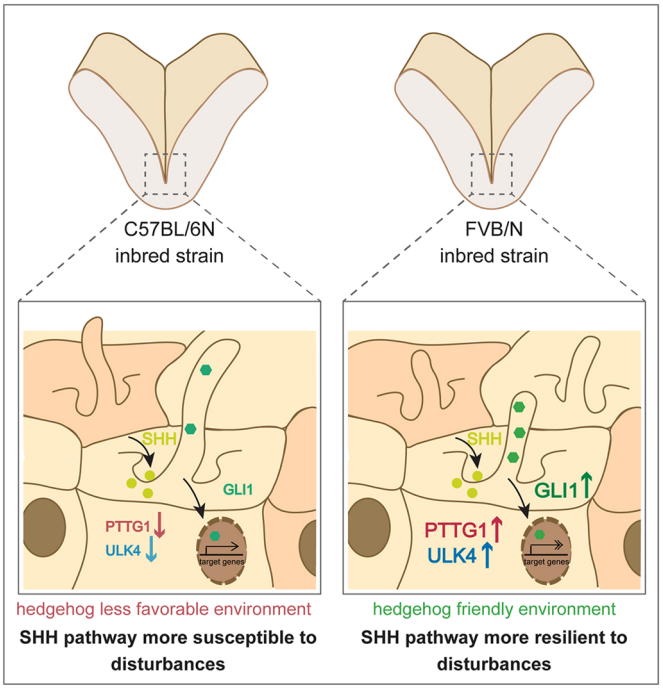

Fig. 8. Proposed model: sufficient SHH signaling is crucial for specification of the developing ventral neural tube and essential for subsequent separation of the cortical hemispheres. Strain-specific expression of candidate modifier genes leaves the neuroepithelial stem cells of C57BL/6N embryos more susceptible to disturbances of the SHH pathway and, therefore, to congenital brain disorders such as HPE. FVB/N neuroepithelial stem cells with higher *Pttg1* and *Ulk4* expression show enhanced SHH signaling and might be more resilient to disturbances of the SHH pathway. ULK4 and PTTG1 are linked to microtubule function, and are both localized to the ciliary axoneme. The levels of the modifiers could enhance microtubule repolymerization of the ciliary axoneme after cell division and thereby facilitate SHH signaling.

Development (2021) 148, dev199307. doi:10.1242/dev.199307

MATERIALS AND METHODS

Animals

Experiments involving animals were performed according to institutional guidelines following approval by local authorities (X9005/12). Mice were housed in a 12 h light-dark cycle with *ad libitum* food and water. The generation of mice with targeted disruption of the *Lrp2* gene has been described before (Willnow et al., 1996). The *Lrp2* mutant mouse line was crossed onto a pure C57BL/6NCrl background in our laboratory (Spoelgen et al., 2005) (herein referred to as *Lrp2* mutant C57BL/6N). For this study, the $Lrp2^{+/-}$ C57BL/6N line was backcrossed for more than 12 generations to obtain a congenic mouse line on a FVB/NCrl background (herein referred to as *Lrp2* mutant on FVB/N background).

We used mice over 8 weeks of age for timed matings for our experiments. Analyses of the congenital defects were carried out in $Lrp2^{-/-}$ and in somite matched $Lrp2^{+/+}$ and/or $Lrp2^{+/-}$ control littermates on a C57BL/6NCrl and FVB/NCrl background. For the generation of the F1 hybrid *Lrp2* mutant embryos, which were used for RNA sequencing experiments, $Lrp2^{+/-}$ FVB/NCrl females were crossed with $Lrp2^{+/-}$ C57BL/6NCrl males. For phenotype analyses on F1 *Lrp2* mutant embryos, $Lrp2^{+/-}$ FVB/NCrl females were crossed with $Lrp2^{+/-}$ C57BL/6NCrl males to generate FVBB6F1 embryos and, conversely, to generate B6FVBF1 embryos. No difference in the phenotypic appearance was observed between these $Lrp2^{-/-}$ F1 mutants. PCR genotyping was performed from yolk sac genomic DNA for E8.5 embryos and from tail biopsies for older embryos.

Histology

Standard Nissel and Hematoxylin and Eosin stainings were performed on paraffin wax-embedded sections. Embryos were fixed in 4% paraformaldehyde in PBS at 4°C, overnight, embedded in paraffin wax and cut at 10 µm. Nissl staining was performed in 0.1% Cresol Red solution (Sigma Aldrich, 114480) for 3-10 min. Hematoxylin and Eosin staining was performed according to manufacturer's instructions with incubation times of 5 min in Hematoxylin (Carl Roth, T865) and 3 min in Eosin (Carl Roth, X883.2). Sections were dehydrated and mounted in Roti Histokit (Carl Roth, 6638.1). Staining was visualized using the Leica DM5000B microscope with LAS-X 3.3.3 software.

In situ hybridization

Whole-mount *in situ* hybridization was carried out as described previously (Hammes et al., 2001). *In situ* hybridization on sections was performed as described previously (Jensen and Wallace, 1997), except that the signal was enhanced by performing the color reaction in the presence of 10% poly vinyl alcohol (Sigma Aldrich, P8136). Probe synthesis was conducted with the components of the DIG RNA labeling kit (Roche, 11277073910). Plasmids for generating *in situ* probes were generated from the following mRNA sequences: *Nkx2.1* (NM_009385.3, bp 2032-2813) kindly provided by Carmen Birchmeier (MDC, Berlin, Germany) and *Shh* (NM_009170.3, bp 455-1097) kindly provided by Andrew P. McMahon (University of Southern California, Los Angeles, USA). Images of embryonic heads were taken using a Leica MZ 10F stereomicroscope (Leica LAS V4.9 imaging software). Images were processed with the Adobe Photoshop select and mask tool to isolate embryonic heads and adjust the background color.

Labeling of heart samples with Batson's pigment

Polymeric dye injections were used to visualize the ascending aorta and the pulmonary artery in isolated E18.5 mouse hearts applying the Batson's #17 Anatomical Corrosion Kit (Polyscience, 07349). Batson's #17 Blue pigment was added to Base Solution A at 2%, mixed vigorously and divided into two equal parts. 24 ml of the Catalyst was added to the first 100 ml of Base Solution A/pigment mix. 24 drops of Promoter C were carefully added to the second half of the Base Solution A/pigment and mixed slowly. Both solutions were mixed together and stirred. After both parts were mixed, it took 30-45 min until the solution was fully polymerized and until then the experiment was finished. The same procedure was repeated for Batson's #17 Red pigment. Injections of the blue and red pigment solution into the right and left ventricle, respectively, were made with a disposable polyethylene syringe and 23 G needle under a stereomicroscope (Leica MZ 10F). Images of the heart were taken after the injection (Leica LAS V4.9 imaging software).

RNA library generation and sequencing

For the generation of an RNA library, embryonic heads of E9.5 embryos were dissected, snap frozen and stored at −80°C until RNA isolation. RNA was extracted using RNeasy Plus Micro kit (Qiagen, 74034), checked on Bioanalyzer (Agilent RNA 6000 Nano kit, 5067-1511) and samples with RIN>9 were used to prepare the cDNA library. Library preparation for mRNA sequencing was performed according to the Illumina SR TruSeq Stranded mRNA protocol (Cluster Kit V3, Illumina, 20020594) on 23 embryonic head RNA samples from mice with 24 somites. Sequencing was performed on the Illumina HiSeq2000 system with HCS 2.2.38 software.

Sequencing reads were aligned to a SNP-infused (FVB/NCrl and C57BL/6NCrl SNPs, accordingly) mouse genome (Ensembl GRCm38.77) using TopHat v2.0.12 with Bowtie 2.0.6.0. The number of reads that mapped to a gene was counted using the HTseq-count v0.6.0 with default parameters. All expressed genes (n=10,861) have been used for differential expression analysis using DESeq2 v1.12.4 (Love et al., 2014). We defined genes as differentially expressed if they met our significance threshold of FDR≤0.05. Allele-specific expression was determined by counting the reads matching the C57BL/6N or FVB/N genotype in the F1 mRNA-seq data.

Differential gene expression analysis

mRNA-seq quantifications were derived from exon-mapped, paired-end reads. Expression quantification was followed by read normalization, size factor estimation and differential expression analysis using DESeq2 v1.12.4 (Love et al., 2014).

For this analysis, we included all genes that we consider to be expressed, defined as having at least 100 reads in 23 out of 26 samples (n=10,861). We considered a gene to be differentially expressed when it met genome-wide significance thresholds of FDR≤0.05. We performed three different comparisons: (1) genotype comparison, where we assessed expression differences for each mouse strain separately (C57BL/6N, FVB/N or the F1 strain), comparing $Lrp2^{-/-}$ versus $Lrp2^{+/+}$ samples; (2) strain comparison, where the different mouse strains, C57BL/6N versus FVB/N and F1, were compared in $Lrp2^{+/+}$ and $Lrp2^{-/-}$ samples; and (3) the interaction of genotype and strain effects, where the interplay of strain and LRP2 deficiency was assessed to understand strain differences that were observed between $Lrp2^{+/+}$ versus $Lrp2^{-/-}$ samples.

Real-time quantitative reverse transcription PCR (real-time qRT-PCR)

Total RNA from E9.5 embryos heads was isolated using RNeasy Plus Micro kit (Qiagen, 74034). RNA from NIH-3T3 and hTERT RPE-1 cells was extracted using TRIzol Reagent (Thermo Fisher, 15596026). cDNA was synthesized by high-capacity RNA-to-cDNA kit (Thermo Fisher, 4387406). Quantitative PCR was performed using TaqMan Universal PCR Master Mix (Thermo Fisher, 4304437) with the BioRad CFX384 Real Time System used on a BioRad C1000 Touch Thermal Cycler. The following TaqMan probes were used: *Gli1* (mouse, Thermo Fisher, assay ID: Mm00494654_m1), *Ptg1* (mouse, Thermo Fisher, assay ID: Mm00479224_m1), *Ulk4* (mouse, Thermo Fisher, assay ID: Mm01349658_m1), *PTTG1* (human, Thermo Fisher, assay ID: Hs00851754_u1) and *ULK4* (human, Thermo Fisher, assay ID Hs00296985_m1). The expression of genes was normalized to *Gapdh* (mouse, Thermo Fisher, assay ID: Mm99999915_g1) or *GAPDH* (human, Thermo Fisher, assay ID Hs99999905_m1). Transcript levels relative to *Gapdh* were calculated using the deltaCt method. Data were analyzed in GraphPad Prism 7 using an unpaired *t*-test or ANOVA. The method is indicated in the figure legends.

Cell culture

The NIH-3T3 and HEK293T cell lines were obtained from T. Willnow (MDC, Berlin, Germany) (Christ et al., 2012). SHHN-293 cells were originally kindly provided by M. Kato (Stanford School of Medicine, CA,

Development (2021) 148, dev199307. doi:10.1242/dev.199307

USA). Cells were maintained in DMEM (Invitrogen, 31966047) with 10% fetal bovine serum (FCS, PAN-Biotech, P40-37500) and 1% penicillin-streptomycin (Invitrogen, 15140122). Human cell line hTERT RPE-1 (ATCC CRL4000) was purchased from the American Type Culture Collection (ATCC, 70021355). Cells were maintained in DMEM: F12 Medium (ATCC 302006) with 10% fetal bovine serum (FCS, PAN-Biotech, P40-37500) containing 0.01 mg/ml hygromycin B (Santa Cruz, sc-506168).

All cell cultures were free of contamination. hTERT RPE-1 cells were purchased from ATCC in July 2020 and certified to be free of mycoplasma contamination.

For overexpression experiments, NIH-3T3 cells were transfected with Lipofectamine 3000 Transfection Reagent (Invitrogen, L3000015) according to the manufacturer's instructions. The following overexpression constructs were used: cDNA *Pttg1* (Origene, MR202008), cDNA *Ulk4* (Origene, MR217918), *B9d1* RIKEN cDNA clone (Source Bioscience, 0710008G05), *Tuba1c* RIKEN cDNA clone (Source Bioscience, 2810407E13). Following 24 h transfection, NIH-3T3 cells were stimulated for 48 h with conditioned medium from HEK293 cells stably secreting SHH-Np (SHHN-293 cells; kindly provided M. Kato, Stanford School of Medicine, CA, USA) or control medium from parental HEK293T cells, at a 1:10 dilution, unless stated otherwise.

The hTERT RPE-1 cells were transfected with TransIT-LT1 Transfection Reagent (Mirus, MIR2304) according to the manufacturer's instructions. 24 h after transfection, hTERT RPE-1 cells were serum starved for 24 h to promote cilia formation and then stimulated for 48 h with conditioned medium from HEK293 cells stably secreting SHH-Np or control medium, at a 1:10 dilution.

ULK4, PTTG1 and B9D1 silencing was achieved by siRNA transfection. NIH-3T3 or hTERT RPE-1 cells were transfected using Lipofectamine RNAiMAX (Thermo Fisher, 13778-150) for the western blot and/or qPCR experiments. NIH-3T3 cells were transfected using DharmaFECT Duo Transfection Reagent (Horizon, T-2010-02) for the dual luciferase reporter assay. The following siRNA was used at final 50 nM concentration in NIH-3T3 cells: *Ulk4* (Thermo Fisher, AM16708, Assay ID: 168185), *Pttg1* (Thermo Fisher, 4390771, Assay ID: s78255), *B9d1* (Thermo Fisher, 4390771, Assay ID: s77534) and negative control (Thermo Fisher, 4390847). The following siRNA was used at final concentration of 40 nM in hTERT RPE-1 cells: *ULK4* (Thermo Fisher, 4390824, Assay ID: s29923), *PTTG1* (Thermo Fisher, 4390820, Assay ID: s17653). Prior to the final assay, cells were subjected to the SHH stimulation with conditioned medium using the same method as for overexpression experiments described above. The knockdown was validated using western blot or qPCR (see Fig. S5).

Dual luciferase reporter assay

NIH-3T3 cells, seeded in 24-well plates, were transiently co-transfected with the gene of interest or a completely empty plasmid, GLI-dependent firefly luciferase reporter (8×3′Gli-BSδ51LucII) (Sasaki et al., 1997) and a constitutive Renilla luciferase reporter (pRL-TK; Promega, E2241) at a ratio of 10:10:1. In the knockdown experiments, 50 nM siRNA targeting gene of interest or a negative control siRNA was used. 24 h later, the medium was replaced with conditioned medium from HEK293 cells stably secreting SHH-Np (SHHN-293 cells; kindly provided M. Kato, Stanford School of Medicine, CA, USA) or control medium from parental HEK293T cells, at a 1:10 dilution or 1:20 dilution (low SHH), in medium containing 0.5% FCS. For the control studies KAAD-cyclopamine (Calbiochem, 239804) at a 50 nM concentration or solvent was added to the conditioned medium with SHH-Np.

After 48 h of stimulation, activity was assayed with D-luciferin (ZellBio, LUCK-100) and results were normalized to the corresponding Renilla activity, assayed with coelenterazine (ZellBio, CZ2.5). For Dual Luciferase reporter assay measurements, a Centro XS^3 LB 960 Microplate Luminometer (Berthold Technologies) and MikroWin 2000 4.41 software (Mikrotek Laborsysteme) was used. Experiments were performed in triplicate, referring to three different wells assayed the same day, in minimum of three independent experiments; results are shown as mean±s.d. Statistical analyses were performed using two-way ANOVA with Dunnett's multiple comparisons test.

Western blot analysis

E8.5 whole embryos were lysed in SDS lysis buffer [60 mM Tris-HCl (pH 6.8), 2% SDS, 10% glycerol, 0.01% Bromophenol Blue and 1.25% β-mercaptoethanol). Samples were heated to 95°C for 5 min, centrifuged for 2 min at 16,363 ***g*** and stored at −20°C until used. Cells were lysed in the RIPA lysis buffer [20 mM Tris-HCl (pH 7.5), 150 mM NaCl, 1 mM Na_2EDTA, 1 mM EGTA, 1% NP-40, 1% sodium deoxycholate and 1 mM AEBSF]. Equal amounts of samples were subjected to a Tris-Glycine Gel (Invitrogen, XP0012C) in a Mini Gel Tank (Invitrogen, A25977). The resolved proteins were transferred onto a nitrocellulose membrane (Amersham Protran 0.2 µm, 10600006) using a wet electroblotting system (Bio-Rad Mini Protean II Cell) followed by immunoblotting. For GLI1 detection, transfer without methanol was performed. 5% non-fat dry milk in TBS-T (0.1% Tween-20) was used for blocking at room temperature for 1 h. Primary antibodies were used overnight at 4°C as follows: rabbit anti-PTTG1 (Abcam, ab79546, 1:5000, knockout validated by Abcam and knockdown validated in this work, see Fig. S5), mouse anti-alpha Tubulin (Merck Millipore, CP06, 1:2000), mouse anti-GLI1 (Cell Signaling, 2643S, 1:1000), rabbit anti-HSP90 (Cell Signaling, 4874S, 1:1000), rabbit anti-ULK4 (Novus Biologicals, NBP1-20229, 1:2000, knockdown validated in this work, see Fig. S5 and Lang et al., 2014) and mouse anti-GAPDH (Santa Cruz, sc32233, 1:5000). Signal was detected by SuperSignal West Dura (Life Technologies, 34075) with an Optimax 2010 X-Ray Film Processor (PROTECT) or using the BioRad ChemiDoc MP Imaging System. The results were quantified using ImageJ, with one-way ANOVA or unpaired *t*-test as a statistical analysis.

Sample preparation for confocal microscopy

Immunofluorescence on sections

Standard immunofluorescence was performed on cryo- and paraffin sections. For cryosections, PFA fixed embryos were infiltrated with 15% and 30% sucrose in PBS for up to 24 h depending on the stage, embedded in OCT (Tissue-Tek, Sakura Finetek, sa-4583) and cut into 10 µm coronal sections. For paraffin wax-embedded sections PFA fixed embryos were dehydrated, incubated in RotiHistol (Carl Roth, 6640.1), embedded in paraffin wax and cut into 10 µm sections. Standard immunohistochemical analysis was carried out by incubation of tissue sections with primary antibodies at the following dilutions: rabbit anti-SHH (Santa Cruz, sc9024, 1:50), sheep anti-LRP2 antiserum (1:4000; kindly provided by the Laboratory of Renata Kozyraki, INSERM, University of Paris, France) rabbit anti-LRP2 (Abcam, ab76969, 1:1000) and rabbit anti-PTTG1 (Abcam, ab79546, 1:100, knockout validated by Abcam). Bound primary antibodies were visualized using secondary antisera conjugated with Alexa Fluor 488, 555 and 647 (1:500, Abcam). All samples were counterstained with DAPI (Invitrogen, 62248). Sections were mounted with Dako Fluorescence Mounting Medium (Agilent, S302380-2).

Immunocytochemistry

For immunocytochemistry, NIH-3T3 cells were seeded in chamber slides (Sigma, C6807) in regular 10% FCS/DMEM medium conditions. After 24 h, cells were rinsed with 1×PBS fixed with 4% PFA for 15 min at room temperature and permeabilized with PBS-TritonX 0.25% for 20 min. Blocking with 10% donkey serum/PBS-TritonX for 1 h, was followed by a standard incubation with primary and secondary antibodies, as described above. Primary antibodies were used at the following dilutions: rabbit anti-SMO (kindly provided by Thomas Willnow, MDC, Berlin, Germany; 1:400), mouse anti-SMO (Santa Cruz, sc166685, 1:200), rabbit anti-ULK4 (Novus Biologicals, NBP1-20229, 1:200; knockdown validated in this work, see Fig. S5 and by Lang et al., 2014), rabbit anti-PTTG1 (Abcam, ab79546, 1:100, knockout validated by Abcam and knockdown validated in this work, see Fig. S5), goat anti-PTTG1 (LifeSpan Biosciences, LS-B5119-50, 1:100, validated for IF, IHC and Peptide-ELISA), mouse anti-ARL13b (UC Davis/NIH NeuroMab, 75-287, 1:500), rabbit anti-ARL13b (ProteinTech, 17711-1-AP, 1:1500), mouse anti-acetylated Tubulin (Sigma, T7451, 1:1000) and mouse anti-γTubulin (Sigma, T6557, 1:200). Walls from the chambers were disassembled according to manufacturer's instruction and samples were mounted with Dako Fluorescence mounting medium. Each experiment was repeated at least five times in triplicate.

Development (2021) 148, dev199307. doi:10.1242/dev.199307

For immunocytochemistry, hTERT RPE-1 cells were seeded on cover slips (Paul Marienfeld, 0111520). After 48 h, cells were rinsed with 1×PBS and fixed in 4% PFA for 15 min at room temperature. Permeabilization and antibody staining was performed as described for NIH-3T3.

Preparation of mouse cephalic explants for immunofluorescence analysis

Explants were prepared analogically as described previously (Echevarria et al., 2002). E9.5 mouse embryos were collected and the neural tube was cut open along the dorsal midline, from a caudal to rostral direction, using an insect needle. The neural folds were precisely cut above the heart and placed on the sterile filter (Millipore, MCEP06H48) on the Petri dish in the drop of 1×PBS. The floor plate at the level of the cephalic flexure was pinched in order to unfold the tissue with the ventricular part facing up. A filter was placed in the six-well plate containing DMEM/10% FCS and explants were incubated at 37°C, with 5% CO_2 and 95% humidity for 3-4 h to flatten and recover. The explants were washed gently in 1×PBS, fixed 1 h in 4% PFA, and subjected to the standard immunofluorescence protocol described above, with 2 nights of primary antibody incubation, as follows: rabbit anti-PTTG1 (Abcam, ab79546, 1:100), goat anti-PTTG1 (LifeSpan Biosciences, LS-B5119-50, 1:100), mouse anti-ARL13b (UC Davis/NIH NeuroMab, 75-287, 1:500). Secondary antibodies conjugated with Alexa Fluor 488 were used to visualize primary cilia and secondary antibodies conjugated with Alexa Fluor 647 were used to visualize PTTG1 signals. Explants were flat mounted in Slow Fade Diamond Antifade Mountant (Invitrogen, S36963) using Secure-Seal Spacer (Invitrogen, S24737) in order to match the refractive index (RI) of the mountant and the immersion media of the glycerol objective, and to prevent distortions of the explant by pressure, shrinking and hardening of the mountant.

Confocal microscopy image acquisition

Image acquisitions of tissue sections were carried out using either a Leica SPE or Leica TCS SP8 confocal microscope using a HC Pl Apo 20× NA 0.75 MultiIMM and HC Pl Apo 63× NA 1.3 oil immersion objective. All samples that were compared either for qualitative or quantitative analysis were imaged under identical settings for laser power, detector and pixel size. NIH-3T3 cells were imaged with a Leica TCS SP5 or Leica TCS SP8 confocal microscope equipped with a ACS Apo 63× oil NA 1.3 immersion objective. hTERT RPE-1 cells were imaged with Zeiss LSM 700 confocal microscope equipped with a plan-Apo 63x 1.4 oil immersion objective.

The forebrain region of the explant samples was imaged en face with a Leica TCS SP8 confocal microscope using a HC Pl Apo 63× NA 1.3 glycerol immersion objective with a working distance of 0.3 mm to enable high-resolution imaging with minimal spherical aberrations of the thick specimen. Three regions per explants were imaged for n=6 C57BL/6N and n=6 FVB/N. High-resolution z-stack (60 nm pixel size, 12 bit, 0.2 µm z-step size) images of apical side of neuroepithelium were acquired with a z-piezo stepper. In all samples, Alexa Fluor 488 was excited by a 488 nm laser, detection at 500-550 nm, Alexa Fluor 555 was excited by a 555 nm laser, detection at 570-620 nm, Alexa Fluor 647 was excited by a 633 nm or 647 nm laser, detection at 660-730 nm, and DAPI was excited at 405 nm, detection at 420-450 nm with a pinhole set to 1 AU.

Image processing and analysis

3D data processing, deconvolution and correction

Confocal z-stacks of explants were subjected to a background correction and processed by deconvolution with the CMLE algorithm in order to obtain an improved signal-to-noise ratio, and axial and spatial resolution using Huygens Professional 19.10 software (Scientific Volume Imaging). For optimal deconvolution, the experimental PSF was calculated with Huygens PSF Distiller by using sub-resolution TetraSpeck Microspheres, 0.2 µm (Invitrogen, T7280) embedded and acquired with same imaging conditions as the explant sample. The same deconvolved beads sample was used to estimate a chromatic aberration correction matrix (in x/y/z) which was used to correct the experimental sample data. To obtain isotropic voxel values, the aspect ratio of the deconvolved bead sample was changed. This new sampling value was applied to all image data with the IMARIS Software before carrying out further segmentation and analysis steps.

Immunofluorescence signal localization analysis

Localization of the protein of interest (PTTG1) within the primary cilium of mouse neuroepithelium was assessed using IMARIS software (Imaris 9.3 and 9.5, Bitplane) after applying raw data corrections (deconvolution, chromatic shift correction and non-isotropic imaging correction). 3D rendering and surfaces reconstruction of individual cilia was performed for two channels – one for cilia marker (ARL13b) and one for PTTG1 – and the classical object-based colocalization approach (individual segmentation and voxel based colocalization) with IMARIS XT module was used. To visualize the precise spatial co-existence of the two proteins in individual cilia, views from different angles were created and transparent LUTs as well as clipping planes were used to cut the 3D surfaces open to enable visualization of inside the cilia. Total number of cilia in each sample was assessed during the same processing steps from the reconstructed surface of ARL13b signal, and was given as number of cilia per area (Fig. S7B).

Quantification of immunofluorescence signal intensity

Z-stack images of the coronal sections were analyzed using ImageJ (Fiji, NIH). For the quantification of PTTG1 signals in the neuroepithelium, the full z-stack was used. The region of interest (ROI) was manually outlined as shown in Fig. S4C and the mean fluorescent intensity was measured with the ROI manager. The average intensity for each animal was used in the final quantification and one-way ANOVA statistical analysis was performed to assess the significance.

For the ciliary SMO fluorescence intensity quantification, z-stack images from NIH-3T3 cells were subjected to the background subtraction and semi-automated threshold adjustment of SMO signals. The mean signal intensity was referred to as ciliary only when directly related to the γ-tubulin-positive ciliary base. The experiment was performed in triplicate referring to three separate wells. One-way ANOVA statistical analysis was performed.

Immunofluorescence analysis of primary cilia using STED microscopy imaging

En face single-color stimulated emission depletion (STED) microscopy imaging was performed on the mouse cephalic explants, which were prepared as described above, with the exception that the highly cross-absorbed secondary antibody Alexa Fluor Plus 594 (Invitrogen, A32744) and ProLong Gold Antifade mountant (Invitrogen, P36934) were used to obtain optimal resolution. STED microscopy images were taken with a Leica SP8 TCS STED microscope (Leica Microsystems) equipped with a pulsed white-light excitation laser (WLL; ∼80 ps pulse width, 80 MHz repetition rate (NKT Photonics) and two STED laser for depletion at 592 nm and 775 nm. The system was controlled by the Leica LAS X software. Single-color STED imaging was performed by exciting Alexa Fluor Plus 594 at 594 nm and the depletion of its emission with the 775 nm STED laser. Time-gated detection was set from 0.3 to 6 ns. The fluorescence signal was detected from 604 to 650 nm by a hybrid detector (HyD) at appropriate spectral regions separated from the STED laser. Images were acquired with a HC PL APO CS2 100×/1.40 NA oil objective (Leica Microsystems), a scanning format of 1024×1024 pixels, 8-bit sampling, 16× line averaging and 6× optical zoom, yielding a pixel size of 18.9×18.9 nm. Additionally, for every STED image, a confocal image with the same settings but only 1× line averaging was acquired.

All STED microscope images of the cilia within each independent experiment were acquired with equal settings. Single optical plane images were subjected to the cilia length quantification in ImageJ. Regions of interest (ROIs) were manually selected with the segmented line tool and the total lengths of single cilia were measured. The average cilia lengths for both mouse lines were checked for the statistical significance using an unpaired t-test.

Scanning electron microscopy

For scanning electron microscopy, E8.5 embryos were dissected and fixed in 0.1 M sodium cacodylate buffer (pH 7.3/7.4) containing 2.5% glutaraldehyde. After rinsing in cacodylate buffer, a post-fixation step of 2% OsO_4 for 2 h followed. Samples were dehydrated in a graded ethanol

series, osmicated, dried in critical point apparatus Polaron 3000, coated with gold/palladium MED 020 (BAL-TEC) and examined using a Zeiss scanning electron microscope (Gemini DSM 982).

Transmission electron microscopy and immunogold labeling

The head region of mouse embryos at E9.5 was fixed with 3% freshly prepared formaldehyde/0.05% glutaraldehyde (EM grade) in 0.1 M phosphate buffer for 1 h at room temperature. After washing, samples were infiltrated with 2.3 M sucrose overnight at 4°C and frozen. Semi-thin sections were prepared to identify the region of the neuroepithelium. Ultrathin 100 nm cryosections according to Tokuyasu were labeled with knockout-validated anti-PTTG1 antibody (Abcam, ab79546, diluted 1:50) or anti-ULK4 antibody (Novus Biologicals, NBP1-20229, 1:300), and 12 nm colloidal gold anti-rabbit secondary antibody (Dianova, 111-205-144). Sections were contrasted and stabilized with a mixture of 3% tungstosilicic acid hydrate and 2.5% polyvinyl alcohol. EM pictures were taken at 80 kV with a Morgagni electron microscope (Thermo Fisher), equipped with a Morada camera and the iTEM software (EMSIS, Münster, Germany).

Quantification and statistical analysis

Tests used to analyze the data were carried out using Prism 7 software (GraphPad) and are mentioned in the respective figure legends. Figures were prepared using Adobe Illustrator 2019 software.

The term significant was used if $P<0.05$. Exact P values, n numbers and biological replicates are reported in the figure legends, supplementary tables or appropriate section in the Materials and Methods.

Acknowledgements

We are grateful to Manfred Ströhmann for excellent work in mouse husbandry. We thank Anke Scheer for excellent technical assistance. Wei Chen and Mirjam Feldkamp (MDC genomics platform) performed RNA deep sequencing. Alexandra Klaus-Bergmann provided helpful discussions. Petra Schrade helped with scanning electron microscopy. Christina Schiel performed immunogold electron transmission microscopy. We thank Thomas Willnow for acquisition of financial support. We thank Gary Lewin for helpful discussions, intellectual input, critical reading of the manuscript and for additional salary support. We are grateful to David Mick and Kerstin Feistel for critically reading the manuscript and for intellectual input.

Competing interests

The authors declare no competing or financial interests.

Author contributions

Conceptualization: A.H.; Methodology: M.L., M.R., A.S., B.P., N.H.; Formal analysis: M.L., M.R., A.S.; Investigation: N.M., I.K., F.W., J.G., A.L., T.M.M., H.G., B.P., A.H.; Resources: N.H.; Writing - original draft: A.H.; Visualization: N.M., I.K.; Supervision: A.H.; Project administration: A.H.; Funding acquisition: A.H.

Funding

Funding was provided by the Deutsche Forschungsgemeinschaft (SFB665, SFB958 and GRK2318/1). Open access funding provided by the Max-Delbruck-Centrum fur Molekulare Medizin in der Helmholtz-Gemeinschaft. Deposited in PMC for immediate release.

Data availability

Raw RNA sequencing datasets have been deposited in the European Nucleotide Archive (ENA) at EMBL-EBI under accession number PRJEB46911.

Peer review history

The peer review history is available online at https://journals.biologists.com/dev/article-lookup/doi/10.1242/dev.199307

References

Anderson, R. M., Lawrence, A. R., Stottmann, R. W., Bachiller, D. and Klingensmith, J. (2002). Chordin and noggin promote organizing centers of forebrain development in the mouse. *Development* **129**, 4975-4987. doi:10.1242/dev.129.21.4975

Baardman, M. E., Zwier, M. V., Wisse, L. J., Groot, A. C. G., Kerstjens-Frederikse, W. S., Hofstra, R. M. W., Jurdzinski, A., Hierck, B. P., Jongbloed, M. R. M., Berger, R. M. F. et al. (2016). Common arterial trunk and ventricular non-compaction in Lrp2 knockout mice indicate a crucial role of LRP2 in cardiac development. *Dis. Model. Mech.* **9**, 413-425. doi:10.1242/dmm.022053

Banting, G. S., Barak, O., Ames, T. M., Burnham, A. C., Kardel, M. D., Cooch, N. S., Davidson, C. E., Godbout, R., McDermid, H. E. and Shiekhattar, R. (2005). CECR2, a protein involved in neurulation, forms a novel chromatin remodeling complex with SNF2L. *Hum. Mol. Genet.* **14**, 513-524. doi:10.1093/hmg/ddi048

Bernal, J. A., Luna, R., Espina, Á., Lázaro, I., Ramos-Morales, F., Romero, F., Arias, C., Silva, A., Tortolero, M. and Pintor-Toro, J. A. (2002). Human securin interacts with p53 and modulates p53-mediated transcriptional activity and apoptosis. *Nat. Genet.* **32**, 306-311. doi:10.1038/ng997

Boelaert, K., Tannahill, L. A., Bulmer, J. N., Kachilele, S., Chan, S. Y., Kim, D., Gittoes, N. J. L., Franklyn, J. A., Kilby, M. D. and Mccabe, C. J. (2003). A potential role for PTTG/securin in the developing human fetal brain. *FASEB J.* **17**, 1631-1639. doi:10.1096/fj.02-0948com

Breslow, D. K., Hoogendoorn, S., Kopp, A. R., Morgens, D. W., Vu, B. K., Kennedy, M. C., Han, K., Li, A., Hess, G. T., Bassik, M. C. et al. (2018). A CRISPR-based screen for Hedgehog signaling provides insights into ciliary function and ciliopathies. *Nat. Genet.* **50**, 460-471. doi:10.1038/s41588-018-0054-7

Briscoe, J. and Thérond, P. P. (2013). The mechanisms of Hedgehog signalling and its roles in development and disease. *Nat. Rev. Mol. Cell Biol.* **14**, 416-429. doi:10.1038/nrm3598

Chiang, C., Litingtung, Y., Lee, E., Young, K. E., Corden, J. L., Westphal, H. and Beachy, P. A. (1996). Cyclopia and defective axial patterning in mice lacking Sonic hedgehog gene function. *Nature* **383**, 407-413. doi:10.1038/383407a0

Chih, B., Liu, P., Chinn, Y., Chalouni, C., Komuves, L. G., Hass, P. E., Sandoval, W. and Peterson, A. S. (2012). A ciliopathy complex at the transition zone protects the cilia as a privileged membrane domain. *Nat. Cell Biol.* **14**, 61-72. doi:10.1038/ncb2410

Christ, A., Christa, A., Kur, E., Lioubinski, O., Bachmann, S., Willnow, T. E. and Hammes, A. (2012). LRP2 is an auxiliary SHH receptor required to condition the forebrain ventral midline for inductive signals. *Dev. Cell* **22**, 268-278. doi:10.1016/j.devcel.2011.11.023

Christ, A., Marczenke, M. and Willnow, T. E. (2020). LRP2 controls sonic hedgehog-dependent differentiation of cardiac progenitor cells during outflow tract formation. *Hum. Mol. Genet.* **29**, 3183-3196. doi:10.1093/hmg/ddaa200

Cole, F. and Krauss, R. S. (2003). Microform holoprosencephaly in mice that lack the Ig superfamily member Cdon. *Curr. Biol.* **13**, 411-415. doi:10.1016/S0960-9822(03)00088-5

Davidson, C. E., Li, Q., Churchill, G. A., Osborne, L. R. and McDermid, H. E. (2007). Modifier locus for exencephaly in Cecr2 mutant mice is syntenic to the 10q25.3 region associated with neural tube defects in humans. *Physiol. Genomics* **31**, 244-251. doi:10.1152/physiolgenomics.00062.2007

Davie, S. A., Maglione, J. E., Manner, C. K., Young, D., Cardiff, R. D., MacLeod, C. L. and Ellies, L. G. (2007). Effects of FVB/NJ and C57Bl/6J strain backgrounds on mammary tumor phenotype in inducible nitric oxide synthase deficient mice. *Transgenic Res.* **16**, 193-201. doi:10.1007/s11248-006-9056-9

Dubourg, C., Kim, A., Watrin, E., de Tayrac, M., Odent, S., David, V. and Dupé, V. (2018). Recent advances in understanding inheritance of holoprosencephaly. *Am. J. Med. Genet. C Semin. Med. Genet.* **178**, 258-269. doi:10.1002/ajmg.c.31619

Echevarria, D., Vieira, C. and Martinez, S. (2002). Mammalian neural tube grafting experiments: an in vitro system for mouse experimental embryology. *Int. J. Dev. Biol.* **45**, 895-902.

Fabregat, A., Jupe, S., Matthews, L., Sidiropoulos, K., Gillespie, M., Garapati, P., Haw, R., Jassal, B., Korninger, F., May, B. et al. (2018). The reactome pathway knowledgebase. *Nucleic Acids Res.* **46**, D649-D655. doi:10.1093/nar/gkx1132

Fliegauf, M., Benzing, T. and Omran, H. (2007). When cilia go bad: cilia defects and ciliopathies. *Nat. Rev. Mol. Cell Biol.* **8**, 880-893. doi:10.1038/nrm2278

Gajera, C. R., Emich, H., Lioubinski, O., Christ, A., Beckervordersandforth-Bonk, R., Yoshikawa, K., Bachmann, S., Christensen, E. I., Götz, M., Kempermann, G. et al. (2010). LRP2 in ependymal cells regulates BMP signaling in the adult neurogenic niche. *J. Cell Sci.* **123**, 1922-1930. doi:10.1242/jcs.065912

Garcia-Gonzalo, F. R., Corbit, K. C., Sirerol-Piquer, M. S., Ramaswami, G., Otto, E. A., Noriega, T. R., Seol, A. D., Robinson, J. F., Bennett, C. L., Josifova, D. J. et al. (2011). A transition zone complex regulates mammalian ciliogenesis and ciliary membrane composition. *Nat. Genet.* **43**, 776-784. doi:10.1038/ng.891

Geng, X. and Oliver, G. (2009). Pathogenesis of holoprosencephaly. *J. Clin. Invest.* **119**, 1403-1413. doi:10.1172/JCI38937

Geng, X., Speirs, C., Lagutin, O., Inbal, A., Liu, W., Solnica-Krezel, L., Jeong, Y., Epstein, D. J. and Oliver, G. (2008). Haploinsufficiency of Six3 fails to activate Sonic hedgehog expression in the ventral forebrain and causes holoprosencephaly. *Dev. Cell* **15**, 236-247. doi:10.1016/j.devcel.2008.07.003

Genkai, N., Homma, J., Sano, M., Tanaka, R. and Yamanaka, R. (2006). Increased expression of pituitary tumor-transforming gene (PTTG)-1 is correlated with poor prognosis in glioma patients. *Oncol. Rep.* **15**, 1569-1574. doi:10.3892/or.15.6.1569

Gerdes, J. M., Davis, E. E. and Katsanis, N. (2009). The vertebrate primary cilium in development, homeostasis, and disease. *Cell* **137**, 32-45. doi:10.1016/j.cell.2009.03.023

Gerhardt, C., Wiegering, A., Leu, T. and Rüther, U. (2016). Control of Hedgehog signalling by the cilia-regulated proteasome. *J. Dev. Biol.* **4**, 27. doi:10.3390/jdb4030027

Gigante, E. D. and Caspary, T. (2020). Signaling in the primary cilium through the lens of the Hedgehog pathway. *Wiley Interdiscip. Rev. Dev. Biol.* **9**, e377. doi:10.1002/wdev.377

Goetz, S. C. and Anderson, K. V. (2010). The primary cilium: a signalling centre during vertebrate development. *Nat. Rev. Genet.* **11**, 331-344. doi:10.1038/nrg2774

Gromley, A., Yeaman, C., Rosa, J., Redick, S., Chen, C.-T., Mirabelle, S., Guha, M., Sillibourne, J. and Doxsey, S. J. (2005). Centriolin anchoring of exocyst and SNARE complexes at the midbody is required for secretory-vesicle-mediated abscission. *Cell* **123**, 75-87. doi:10.1016/j.cell.2005.07.027

Hagting, A., den Elzen, N., Vodermaier, H. C., Waizenegger, I. C., Peters, J.-M. and Pines, J. (2002). Human securin proteolysis is controlled by the spindle checkpoint and reveals when the APC/C switches from activation by Cdc20 to Cdh1. *J. Cell Biol.* **157**, 1125-1137. doi:10.1083/jcb.200111001

Hammes, A., Guo, J.-K., Lutsch, G., Leheste, J.-R., Landrock, D., Ziegler, U., Gubler, M.-C. and Schedl, A. (2001). Two splice variants of the Wilms' Tumor 1 gene have distinct functions during sex determination and nephron formation. *Cell* **106**, 319-329. doi:10.1016/S0092-8674(01)00453-6

Havens, C. G. and Walter, J. C. (2011). Mechanism of CRL4(Cdt2), a PCNA-dependent E3 ubiquitin ligase. *Genes Dev.* **25**, 1568-1582. doi:10.1101/gad.2068611

Hayhurst, M. and McConnell, S. K. (2003). Mouse models of holoprosencephaly. *Curr. Opin. Neurol.* **16**, 135-141. doi:10.1097/00019052-200304000-00003

He, M., Agbu, S. and Anderson, K. V. (2017). Microtubule motors drive Hedgehog signaling in primary cilia. *Trends Cell Biol.* **27**, 110-125. doi:10.1016/j.tcb.2016.09.010

Hellmuth, S., Gómez-H, L., Pendás, A. M. and Stemmann, O. (2020). Securin-independent regulation of separase by checkpoint-induced shugoshin–MAD2. *Nature* **580**, 536-541. doi:10.1038/s41586-020-2182-3

Heussler, H. S., Suri, M., Young, I. D. and Muenke, M. (2002). Extreme variability of expression of a Sonic Hedgehog mutation: attention difficulties and holoprosencephaly. *Arch. Dis. Child.* **86**, 293-296. doi:10.1136/adc.86.4.293

Heyne, G. W., Everson, J. L., Ansen-Wilson, L. J., Melberg, C. G., Fink, D. M., Parins, K. F., Doroodchi, P., Ulschmid, C. M. and Lipinski, R. J. (2016). Gli2 gene-environment interactions contribute to the etiological complexity of holoprosencephaly: evidence from a mouse model. *Dis. Model. Mech.* **9**, 1307-1315. doi:10.1242/dev.147652

Holt, L. J., Krutchinsky, A. N. and Morgan, D. O. (2008). Positive feedback sharpens the anaphase switch. *Nature* **454**, 353-357. doi:10.1038/nature07050

Hong, M. and Krauss, R. S. (2018). Modeling the complex etiology of holoprosencephaly in mice. *Am. J. Med. Genet. C Semin. Med. Genet.* **178**, 140-150. doi:10.1002/ajmg.c.31611

Jászai, J., Thamm, K., Karbanová, J., Janich, P., Fargeas, C. A., Huttner, W. B. and Corbeil, D. (2020). Prominins control ciliary length throughout the animal kingdom: New lessons from human prominin-1 and zebrafish prominin-3. *J. Biol. Chem.* **295**, 6007-6022. doi:10.1074/jbc.RA119.011253

Jensen, A. M. and Wallace, V. A. (1997). Expression of Sonic hedgehog and its putative role as a precursor cell mitogen in the developing mouse retina. *Development* **124**, 363-371. doi:10.1242/dev.124.2.363

Kantarci, S., Al-Gazali, L., Hill, R. S., Donnai, D., Black, G. C. M., Bieth, E., Chassaing, N., Lacombe, D., Devriendt, K., Teebi, A. et al. (2007). Mutations in *LRP2*, which encodes the multiligand receptor megalin, cause Donnai-Barrow and facio-oculo-acoustico-renal syndromes. *Nat. Genet.* **39**, 957-959. doi:10.1038/ng2063

Karsten, S. L., Kudo, L. C., Jackson, R., Sabatti, C., Kornblum, H. I. and Geschwind, D. H. (2003). Global analysis of gene expression in neural progenitors reveals specific cell-cycle, signaling, and metabolic networks. *Dev. Biol.* **261**, 165-182. doi:10.1016/S0012-1606(03)00274-4

Khalifa, O., Al-Sahlawi, Z., Imtiaz, F., Ramzan, K., Allam, R., Al-Mostafa, A., Abdel-Fattah, M., Abuharb, G., Nester, M., Verloes, A. et al. (2015). Variable expression pattern in Donnai-Barrow syndrome: Report of two novel LRP2 mutations and review of the literature. *Eur. J. Med. Genet.* **58**, 293-299. doi:10.1016/j.ejmg.2014.12.008

Kim, J. C., Ou, Y. Y., Badano, J. L., Esmail, M. A., Leitch, C. C., Fiedrich, E., Beales, P. L., Archibald, J. M., Katsanis, N., Rattner, J. B. et al. (2005). MKKS/BBS6, a divergent chaperonin-like protein linked to the obesity disorder Bardet-Biedl syndrome, is a novel centrosomal component required for cytokinesis. *J. Cell Sci.* **118**, 1007-1020. doi:10.1242/jcs.01676

Kim, A., Savary, C., Dubourg, C., Carré, W., Mouden, C., Hamdi-Rozé, H., Guyodo, H., Douce, J. L., Génin, E., Campion, D. et al. (2019). Integrated clinical and omics approach to rare diseases: novel genes and oligogenic inheritance in holoprosencephaly. *Brain* **142**, 35-49. doi:10.1093/brain/awy290

Kooistra, M. K., Leduc, R. Y. M., Dawe, C. E., Fairbridge, N. A., Rasmussen, J., Man, J. H. Y., Bujold, M., Juriloff, D., King-Jones, K. and McDermid, H. E. (2011). Strain-specific modifier genes of Cecr2-associated exencephaly in mice: genetic analysis and identification of differentially expressed candidate genes. *Physiol. Genomics* **44**, 35-46. doi:10.1152/physiolgenomics.00124.2011

Kowalczyk, I., Lee, C., Schuster, E., Hoeren, J., Trivigno, V., Riedel, L., Görne, J., Wallingford, J. B., Hammes, A. and Feistel, K. (2021). Neural tube closure requires the endocytic receptor Lrp2 and its functional interaction with intracellular scaffolds. *Development* **148**, dev195008. doi:10.1242/dev.195008

Krauss, R. S. (2007). Holoprosencephaly: new models, new insights. *Expert Rev. Mol. Med.* **9**, 1-17. doi:10.1017/S1462399407000440

Krauss, R. S. and Hong, M. (2016). Chapter thirty-three - gene–environment interactions and the etiology of birth defects. In *Current Topics in Developmental Biology* (ed. P. M. Wassarman), pp. 569-580. Academic Press.

Lang, B., Pu, J., Hunter, I., Liu, M., Martin-Granados, C., Reilly, T. J., Gao, G.-D., Guan, Z.-L., Li, W.-D., Shi, Y.-Y. et al. (2014). Recurrent deletions of ULK4 in schizophrenia: a gene crucial for neuritogenesis and neuronal motility. *J. Cell Sci.* **127**, 630-640. doi:10.1242/jcs.137604

Lang, B., Zhang, L., Jiang, G., Hu, L., Lan, W., Zhao, L., Hunter, I., Pruski, M., Song, N.-N., Huang, Y. et al. (2016). Control of cortex development by ULK4, a rare risk gene for mental disorders including schizophrenia. *Sci. Rep.* **6**, 31126. doi:10.1038/srep31126

Leduc, R. Y. M., Singh, P. and McDermid, H. E. (2017). Genetic backgrounds and modifier genes of NTD mouse models: An opportunity for greater understanding of the multifactorial etiology of neural tube defects. *Birth Defects Res.* **109**, 140-152. doi:10.1002/bdra.23554

Li, Y., Klena, N. T., Gabriel, G. C., Liu, X., Kim, A. J., Lemke, K., Chen, Y., Chatterjee, B., Devine, W., Damerla, R. R. et al. (2015). Global genetic analysis in mice unveils central role for cilia in congenital heart disease. *Nature* **521**, 520-524. doi:10.1038/nature14269

Liu, M., Guan, Z., Shen, Q., Lalor, P., Fitzgerald, U., O'Brien, T., Dockery, P. and Shen, S. (2016). Ulk4 Is Essential for Ciliogenesis and CSF Flow. *J. Neurosci. Off. J. Soc. Neurosci.* **36**, 7589-7600. doi:10.1523/JNEUROSCI.0621-16.2016

Longoni, M., Kantarci, S., Donnai, D. and Pober, B. R. (2008). Donnai-Barrow Syndrome. In *GeneReviews* (ed. M. P. Adam, H. H. Ardinger, R. A. Pagon, S. E. Wallace, L. J. Bean, K. Stephens and A. Amemiya), pp. 1993-2021. Seattle, WA: University of Washington, Seattle.

Love, M. I., Huber, W. and Anders, S. (2014). Moderated estimation of fold change and dispersion for RNA-seq data with DESeq2. *Genome Biol.* **15**, 550. doi:10.1186/s13059-014-0550-8

Mei, J., Huang, X. and Zhang, P. (2001). Securin is not required for cellular viability, but is required for normal growth of mouse embryonic fibroblasts. *Curr. Biol.* **11**, 1197-1201. doi:10.1016/S0960-9822(01)00325-6

Ming, J. E. and Muenke, M. (2002). Multiple hits during early embryonic development: digenic diseases and holoprosencephaly. *Am. J. Hum. Genet.* **71**, 1017-1032. doi:10.1086/344412

Mirandola, L., Figueroa, J. A., Phan, T. T., Grizzi, F., Kim, M., Rahman, R. L., Jenkins, M. R., Cobos, E., Jumper, C., Alalawi, R. et al. (2015). Novel antigens in non-small cell lung cancer: SP17, AKAP4, and PTTG1 are potential immunotherapeutic targets. *Oncotarget* **6**, 2812-2826. doi:10.18632/oncotarget.2802

Moreno-Mateos, M. A., Espina, Á. G., Torres, B., del Estal, M. M. G., Romero-Franco, A., Ríos, R. M. and Pintor-Toro, J. A. (2011). PTTG1/securin modulates microtubule nucleation and cell migration. *Mol. Biol. Cell* **22**, 4302-4311. doi:10.1091/mbc.e10-10-0838

Muenke, M. and Beachy, P. A. (2000). Genetics of ventral forebrain development and holoprosencephaly. *Curr. Opin. Genet. Dev.* **10**, 262-269. doi:10.1016/S0959-437X(00)00084-8

Muenke, M. and Cohen, M. M. (2000). Genetic approaches to understanding brain development: Holoprosencephaly as a model. *Ment. Retard. Dev. Disabil. Res. Rev.* **6**, 15-21. doi:10.1002/(SICI)1098-2779(2000)6:1<15::AID-MRDD3>3.0.CO;2-8

Nachury, M. V. and Mick, D. U. (2019). Establishing and regulating the composition of cilia for signal transduction. *Nat. Rev. Mol. Cell Biol.* **20**, 389-405. doi:10.1038/s41580-019-0116-4

Ozdemir, H., Plamondon, J., Gaskin, P., Asoglu, M. R. and Turan, S. (2019). A prenatally diagnosed case of Donnai-Barrow syndrome: Highlighting the importance of whole exome sequencing in cases of consanguinity. *Am. J. Med. Genet. A.* **182**, 289-292. doi:10.1002/ajmg.a.61428

Pan, J., You, Y., Huang, T. and Brody, S. L. (2007). RhoA-mediated apical actin enrichment is required for ciliogenesis and promoted by Foxj1. *J. Cell Sci.* **120**, 1868-1876. doi:10.1242/jcs.005306

Park, T. J., Mitchell, B. J., Abitua, P. B., Kintner, C. and Wallingford, J. B. (2008). Dishevelled controls apical docking and planar polarization of basal bodies in ciliated epithelial cells. *Nat. Genet.* **40**, 871-879. doi:10.1038/ng.104

Petryk, A., Anderson, R. M., Jarcho, M. P., Leaf, I., Carlson, C. S., Klingensmith, J., Shawlot, W. and O'Connor, M. B. (2004). The mammalian twisted gastrulation gene functions in foregut and craniofacial development. *Dev. Biol.* **267**, 374-386. doi:10.1016/j.ydbio.2003.11.015

Pober, B. R., Longoni, M. and Noonan, K. M. (2009). A review of Donnai-Barrow and facio-oculo-acoustico-renal (DB/FOAR) syndrome: Clinical features and

differential diagnosis. *Birt. Defects Res. A. Clin. Mol. Teratol.* **85**, 76-81. doi:10.1002/bdra.20534
Pusapati, G. V., Kong, J. H., Patel, B. B., Krishnan, A., Sagner, A., Kinnebrew, M., Briscoe, J., Aravind, L. and Rohatgi, R. (2018). CRISPR screens uncover genes that regulate target cell sensitivity to the Morphogen Sonic Hedgehog. *Dev. Cell* **44**, 113-129.e8. doi:10.1016/j.devcel.2017.12.003
Read, M. L., Fong, J. C., Modasia, B., Fletcher, A., Imruetaicharoenchoke, W., Thompson, R. J., Nieto, H., Reynolds, J. J., Bacon, A., Mallick, U. et al. (2017). Elevated PTTG and PBF predicts poor patient outcome and modulates DNA damage response genes in thyroid cancer. *Oncogene* **36**, 5296-5308. doi:10.1038/onc.2017.154
Roessler, E. and Muenke, M. (2010). The molecular genetics of holoprosencephaly. *Am. J. Med. Genet. C Semin. Med. Genet.* **154C**, 52-61. doi:10.1002/ajmg.c.30236
Roessler, E., Belloni, E., Gaudenz, K., Jay, P., Berta, P., Scherer, S. W., Tsui, L.-C. and Muenke, M. (1996). Mutations in the human Sonic Hedgehog gene cause holoprosencephaly. *Nat. Genet.* **14**, 357. doi:10.1038/ng1196-357
Roessler, E., Hu, P. and Muenke, M. (2018). Holoprosencephaly in the genomics era. *Am. J. Med. Genet. C Semin. Med. Genet.* **178**, 165-174. doi:10.1002/ajmg.c.31615
Rosenfeld, J. A., Ballif, B. C., Martin, D. M., Aylsworth, A. S., Bejjani, B. A., Torchia, B. S. and Shaffer, L. G. (2010). Clinical characterization of individuals with deletions of genes in holoprosencephaly pathways by aCGH refines the phenotypic spectrum of HPE. *Hum. Genet.* **127**, 421-440. doi:10.1007/s00439-009-0778-7
Sabatino, J. A., Stokes, B. A. and Zohn, I. E. (2017). Prevention of neural tube defects in Lrp2 mutant mouse embryos by folic acid supplementation. *Birth Defects Res.* **109**, 16-26. doi:10.1002/bdra.23589
Salehi, F., Scheithauer, B. W., Sharma, S., Kovacs, K., Lloyd, R. V., Cusimano, M. D. and Munoz, D. G. (2013). Immunohistochemical expression of PTTG in brain tumors. *Anticancer Res.* **33**, 119-122.
Sasaki, H., Hui, C., Nakafuku, M. and Kondoh, H. (1997). A binding site for Gli proteins is essential for HNF-3beta floor plate enhancer activity in transgenics and can respond to Shh in vitro. *Development* **124**, 1313-1322. doi:10.1242/dev.124.7.1313
Schachter, K. A. and Krauss, R. S. (2008). Chapter 3 murine models of holoprosencephaly. *Curr. Top. Dev. Biol.* 84, 139-170. doi:10.1016/S0070-2153(08)00603-0
Shah, A. S., Farmen, S. L., Moninger, T. O., Businga, T. R., Andrews, M. P., Bugge, K., Searby, C. C., Nishimura, D., Brogden, K. A., Kline, J. N. et al. (2008). Loss of Bardet–Biedl syndrome proteins alters the morphology and function of motile cilia in airway epithelia. *Proc. Natl. Acad. Sci. USA* **105**, 3380-3385. doi:10.1073/pnas.0712327105
Sharma, N., Kosan, Z. A., Stallworth, J. E., Berbari, N. F. and Yoder, B. K. (2011). Soluble levels of cytosolic tubulin regulate ciliary length control. *Mol. Biol. Cell* **22**, 806-816. doi:10.1091/mbc.e10-03-0269
Singla, V. and Reiter, J. F. (2006). The primary cilium as the cell's antenna: signaling at a sensory organelle. *Science* **313**, 629-633. doi:10.1126/science.1124534
Smith, K. R., Kieserman, E. K., Wang, P. I., Basten, S. G., Giles, R. H., Marcotte, E. M. and Wallingford, J. B. (2011). A role for central spindle proteins in cilia structure and function. *Cytoskeleton* **68**, 112-124. doi:10.1002/cm.20498
Solomon, B. D., Mercier, S., Vélez, J. I., Pineda-Alvarez, D. E., Wyllie, A., Zhou, N., Dubourg, C., David, V., Odent, S., Roessler, E. et al. (2010). Analysis of genotype–phenotype correlations in human holoprosencephaly. *Am. J. Med. Genet. C Semin. Med. Genet.* **154C**, 133-141. doi:10.1002/ajmg.c.30240
Spektor, A., Tsang, W. Y., Khoo, D. and Dynlacht, B. D. (2007). Cep97 and CP110 suppress a cilia assembly program. *Cell* **130**, 678-690. doi:10.1016/j.cell.2007.06.027
Spoelgen, R., Hammes, A., Anzenberger, U., Zechner, D., Andersen, O. M., Jerchow, B. and Willnow, T. E. (2005). LRP2/megalin is required for patterning of the ventral telencephalon. *Development* **132**, 405-414. doi:10.1242/dev.01580
Taipale, J., Chen, J. K., Cooper, M. K., Wang, B., Mann, R. K., Milenkovic, L., Scott, M. P. and Beachy, P. A. (2000). Effects of oncogenic mutations in Smoothened and Patched can be reversed by cyclopamine. *Nature* **406**, 1005-1009. doi:10.1038/35023008
Tarabykin, V., Britanova, O., Fradkov, A., Voss, A., Katz, L. S., Lukyanov, S. and Gruss, P. (2000). Expression of PTTG and prc1 genes during telencephalic neurogenesis. *Mech. Dev.* **92**, 301-304. doi:10.1016/S0925-4773(00)00243-4
Tekendo-Ngongang, C., Owosela, B., Muenke, M. and Kruszka, P. (2020). Comorbidity of congenital heart defects and holoprosencephaly is likely genetically driven and gene-specific. *Am. J. Med. Genet. C Semin. Med. Genet.* **184**, 154-158. doi:10.1002/ajmg.c.31770
Thornton, B. R. and Toczyski, D. P. (2003). Securin and B-cyclin/CDK are the only essential targets of the APC. *Nat. Cell Biol.* **5**, 1090-1094. doi:10.1038/ncb1066
Tong, Y., Ben-Shlomo, A., Zhou, C., Wawrowsky, K. and Melmed, S. (2008). Pituitary tumor transforming gene 1 regulates Aurora kinase A activity. *Oncogene* **27**, 6385-6395. doi:10.1038/onc.2008.234
van Dam, T. J. P., Wheway, G., Slaats, G. G., Huynen, M. A., Giles, R. H., and **SYSCILIA Study Group**. (2013). The SYSCILIA gold standard (SCGSv1) of known ciliary components and its applications within a systems biology consortium. *Cilia* **2**, 7. doi:10.1186/2046-2530-2-7
Vertii, A., Bright, A., Delaval, B., Hehnly, H. and Doxsey, S. (2015). New frontiers: discovering cilia-independent functions of cilia proteins. *EMBO Rep.* **16**, 1275-1287. doi:10.15252/embr.201540632
Vlotides, G., Eigler, T. and Melmed, S. (2007). Pituitary tumor-transforming gene: physiology and implications for tumorigenesis. *Endocr. Rev.* **28**, 165-186. doi:10.1210/er.2006-0042
Wallis, D. E. and Muenke, M. (1999). Molecular mechanisms of holoprosencephaly. *Mol. Genet. Metab.* **68**, 126-138. doi:10.1006/mgme.1999.2895
Wallis, D. and Muenke, M. (2000). Mutations in holoprosencephaly. *Hum. Mutat.* **16**, 99-108. doi:10.1002/1098-1004(200008)16:2<99::AID-HUMU2>3.0.CO;2-0
Wallis, D. E., Roessler, E., Hehr, U., Nanni, L., Wiltshire, T., Richieri-Costa, A., Gillessen-Kaesbach, G., Zackai, E. H., Rommens, J. and Muenke, M. (1999). Mutations in the homeodomain of the human SIX3 gene cause holoprosencephaly. *Nat. Genet.* **22**, 196-198. doi:10.1038/9718
Wang, L. and Dynlacht, B. D. (2018). The regulation of cilium assembly and disassembly in development and disease. *Development* **145**, dev151407. doi:10.1242/dev.151407
Wang, Z., Yu, R. and Melmed, S. (2001). Mice lacking pituitary tumor transforming gene show testicular and splenic hypoplasia, thymic hyperplasia, thrombocytopenia, aberrant cell cycle progression, and premature centromere division. *Mol. Endocrinol.* **15**, 1870-1879. doi:10.1210/mend.15.11.0729
Wang, L., Piao, T., Cao, M., Qin, T., Huang, L., Deng, H., Mao, T. and Pan, J. (2013). Flagellar regeneration requires cytoplasmic microtubule depolymerization and kinesin-13. *J. Cell Sci.* **126**, 1531-1540. doi:10.1242/jcs.124255
Wang, W., Wu, T. and Kirschner, M. W. (2014). The master cell cycle regulator APC-Cdc20 regulates ciliary length and disassembly of the primary cilium. *eLife* **3**, e03083. doi:10.7554/eLife.03083.019
Weiss, K., Kruszka, P. S., Levey, E. and Muenke, M. (2018). Holoprosencephaly from conception to adulthood. *Am. J. Med. Genet. C Semin. Med. Genet.* **178**, 122-127. doi:10.1002/ajmg.c.31624
Willnow, T. E., Hilpert, J., Armstrong, S. A., Rohlmann, A., Hammer, R. E., Burns, D. K. and Herz, J. (1996). Defective forebrain development in mice lacking gp330/megalin. *Proc. Natl. Acad. Sci. USA* **93**, 8460-8464. doi:10.1073/pnas.93.16.8460
Xiang, W., Wu, X., Huang, C., Wang, M., Zhao, X., Luo, G., Li, Y., Jiang, G., Xiao, X. and Zeng, F. (2017). PTTG1 regulated by miR-146a-3p promotes bladder cancer migration, invasion, metastasis and growth. *Oncotarget* **8**, 664-678. doi:10.18632/oncotarget.13507
Yan, H., Wang, W., Dou, C., Tian, F. and Qi, S. (2015). Securin promotes migration and invasion via matrix metalloproteinases in glioma cells. *Oncol. Lett.* **9**, 2895-2901. doi:10.3892/ol.2015.3074
Yanagida, M. (2000). Cell cycle mechanisms of sister chromatid separation; roles of Cut1/separin and Cut2/securin. *Genes Cells Devoted Mol. Cell. Mech.* **5**, 1-8. doi:10.1046/j.1365-2443.2000.00306.x
Zarbalis, K., May, S. R., Shen, Y., Ekker, M., Rubenstein, J. L. R. and Peterson, A. S. (2004). A focused and efficient genetic screening strategy in the mouse: identification of mutations that disrupt cortical development. *PLoS Biol.* **2**, E219. doi:10.1371/journal.pbio.0020219
Zhang, W., Kang, J.-S., Cole, F., Yi, M.-J. and Krauss, R. S. (2006). Cdo functions at multiple points in the Sonic Hedgehog pathway, and Cdo-deficient mice accurately model human holoprosencephaly. *Dev. Cell* **10**, 657-665. doi:10.1016/j.devcel.2006.04.005
Zheng, Y., Guo, J., Zhou, J., Lu, J., Chen, Q., Zhang, C., Qing, C., Koeffler, H. P. and Tong, Y. (2015). FoxM1 transactivates PTTG1 and promotes colorectal cancer cell migration and invasion. *BMC Med. Genomics* **8**, 49. doi:10.1186/s12920-015-0126-9
Zou, H., McGarry, T. J., Bernal, T. and Kirschner, M. W. (1999). Identification of a vertebrate sister-chromatid separation inhibitor involved in transformation and tumorigenesis. *Science* **285**, 418-422. doi:10.1126/science.285.5426.418
Zuo, X., Guo, W. and Lipschutz, J. H. (2009). The exocyst protein Sec10 is necessary for primary ciliogenesis and cystogenesis in vitro. *Mol. Biol. Cell* **20**, 2522-2529. doi:10.1091/mbc.e08-07-0772
Zywitza, V., Misios, A., Bunatyan, L., Willnow, T. E. and Rajewsky, N. (2018). Single-cell transcriptomics characterizes cell types in the subventricular zone and uncovers molecular defects impairing adult neurogenesis. *Cell Rep.* **25**, 2457-2469.e8. doi:10.1016/j.celrep.2018.11.003